

An extended Kolmogorov–Avrami–Ishibashi (EKAI) model to simulate dynamic characteristics of polycrystalline-ferroelectric-gate field-effect transistors

Shigeki Sakai^{1,2,*} and Mitsue Takahashi^{1,§}

¹*National Institute of Advanced Industrial Science and Technology, 1-1-1, Umezono, Tsukuba, Ibaraki 305-8568, Japan*

²*Research Center for Neuromorphic AI Hardware, Kyushu Institute of Technology, Fukuoka, Japan*

Abstract

An extended Kolmogorov–Avrami–Ishibashi (EKAI) model is proposed, which represents dynamic characteristics in polycrystalline ferroelectric films consisting of grains under time-dependent electric fields. The original Kolmogorov–Avrami–Ishibashi (KAI) model described time-varying polarization reversal in a single-crystal film under a constant electric field. The field and the polarization were directed along the film normal. The polarization reversal dynamics were represented by a time-evolution function, $c(t)$, [Eq. (2) of this paper] regarding the volume fractions of the downward- and upward-polarization domains under a constant electric field. In the EKAI model, a grain in a polycrystalline ferroelectric film is indexed by l with an angle θ_l which is the angle between the spontaneous polarization P_s and the film normal. The EKAI model first assumes KAI-like polarization variations under a constant field inside the grain whose angle is tilted by θ_l . The second assumption is concerned with polarization variation under time-varying electric field. During a time period Δt from t_{now} to $t_{next}(= t_{now} + \Delta t)$, the volume fractions of the downward- and upward-polarization domains changes according to the function $c(t)$ under an electric field at t_{now} . By combining the derived polarization and an electrostatic potential equation across a gate stacked structure at t_{next} , an electric field at t_{next} is derived. Since the electric field and the volume fractions of the downward and upward domains are known at t_{next} , the calculation at the next Δt step is possible. This procedure is repeated, and the EKAI model can simulate time-varying polarization reversal phenomena. The EKAI is applied for simulating quasi-static and dynamic characteristics of ferroelectric gate field-effect transistors (FeFETs) of $(\text{Sr}_{1-x}\text{Ca}_x)\text{Bi}_2\text{Ta}_2\text{O}_9$ (SBT). The SBT FeFETs are suitable for the model verification because they are reproducible with high endurance performance due to fairly small charge injection and trapping in the FeFET gate stacks. Consequent good agreement of the numerical results with the experimental indicates that the EKAI model is appropriate to simulate quasi-static and dynamic characteristics of FeFETs with polycrystalline ferroelectric films under swept and pulsed gate-voltages.

*shigeki.sakai@aist.go.jp

§mitsue-takahashi@aist.go.jp

I. INTRODUCTION

Ferroelectric-gate field-effect transistors (FeFETs) have attracted attention not only by their potential functionality [1,2] such as compact, non-volatile, and non-destructive-read memory cells but also by recent rich accumulations of experimental data. FeFETs have been characterized by various measurements. Quasi-static characteristics of drain current (I_d) *versus* gate voltage (V_g) are measured with slow V_g sweeping by a semiconductor parameter analyzer and a ferroelectric tester. Also, Q_m *vs.* V_g are measured by a quasi-static procedure with the slow V_g sweeping. The Q_m is metal-gate charge density induced by ferroelectric layer polarization. Dynamic time-dependent properties of FeFETs are characterized by a pulse-write-and- V_{th} -read (PWVR; see Fig. 12(b)) or pulse-write-and- I_d -read (PWIR) method. The pulse-write (PW) is done by a pulse generator. In a FeFET, while a positive or negative V_g pulse is given with the V_g height of V_h (> 0) or V_l (< 0), ferroelectric polarization responds dynamically as a function of pulse height (V_h or $-V_l$) and time width (t_w). After ceasing PW, considerable amounts of ferroelectric polarization are retained due to ferroelectricity. This retained polarization is a function of V_h , V_l and t_w . A read operation is done after PW, where V_g of the transistor is swept in a narrow voltage range slowly compared to the PW time scale. A threshold voltage (V_{th}) is read for PWVR, and the drain current (I_d) is read at a fixed V_g for PWIR. A threshold voltage difference (ΔV_{th}) for PWVR or a current ratio between the high- and low- I_d -current states for PWIR can be derived for a pair of the write voltages, V_h and V_l . ΔV_{th} by PWVR or the I_d ratio by PWIR is a performance indicator of an FeFET as a nonvolatile memory transistor.

A lot of experimental results by PWVR and PWIR are available to investigate dynamic polarization switching in metal-ferroelectric-insulator-semiconductor (MFIS) type FeFETs, whose ferroelectric is $\text{SrBi}_2\text{Ta}_2\text{O}_9$ or $(\text{Sr}_{1-x}\text{Ca}_x)\text{Bi}_2\text{Ta}_2\text{O}_9$ [3–6]. The former and the latter are abbreviated as SBT and CSBT, respectively. The SBT and CSBT belong to a family of Bi-layered perovskite oxides with similar electrical properties. The coercive field of CSBT for $x = 0.1 - 0.2$ is 10 % larger than that of SBT. Hereafter FeFETs comprising of SBT or CSBT in the ferroelectric layers are called SBT-FeFETs. The electric properties of SBT-FeFETs are suitable for the model verification because they are reproducible with high switching endurance due to negligibly small charge injection and trapping in the FeFET gate stacks.

Despite the many experimental works of PWVR and PWIR reported in detail, there have been no correct theories based on physics for simulating them. As one of the existing models, a phenomenological Landau-Ginzburg-Devonshire (LGD) theory in ferroelectrics constructs a Gibbs free energy for the ferroelectrics where the primary energy term is expressed as a polynomial expansion form of polarization as an order parameter [7–9]. By minimizing the free energy, equilibrium or quasi-static properties are derived. The LGD theory described the transition between the paraelectric and ferroelectric phases with temperature variation across the Curie temperature [8]. It also described phase transitions between the tetragonal and

orthorhombic and between the orthorhombic and rhombohedral in BaTiO₃, a cubic-based ferroelectric material [7]. In the Gibbs free energy, the spatial differentiation term brought non-homogeneity, by which domain patterns were described [10, 11]. The Gibbs energy for ferroelectrics can include the elastic energy term and the coupling terms of elasticity and polarization since the polarization accompanies lattice displacement of crystals. In a particular case that the ferroelectric film is divided into LGD segments, the LGD theories are called phase field models [12, 13]. The models showed coexistence of 180°- and non-180° domains under constraints of substrates [12], and polycrystalline grain growth [14].

The LGD theory has its own representation of time dependence. In the case that the electric properties without elastic terms are matters of concern, the description of time dependence is sometimes called Landau-Khalatnikov (LK) equation [15–17]. In the phase-field models, it is called the time-dependent Ginzburg-Landau (TDGL) equation [12,18]. LK and TDGL are essentially the same. Lagrangian function, which includes a simple viscosity term of classical mechanics [19], may help us comprehensive understanding the origin of the time-dependent polarization switching. The Gibbs free energy for the ferroelectrics replaces the potential term in the Lagrangian. In deriving equations of motion, the inertia term is usually neglected for polarization reversal problems, and the LK- and TDGL-equation are obtained [20]. Overdamped (*i.e.*, strong viscosity) cases in the Lagrangian may allow us to omit the inertia term in the equation of motion. Despite the long history of theoretical studies about ferroelectric polarization switching, there are no reports which quantitatively explained the experimental PWVR and PWIR of FeFETs. In the case of LK, for example, the time-dependent form seems simplified but makes difficulties in fitting the model to the experimental. In the case of TDGL, in which ferroelectric films are separated by many segments, calculation and parameter optimization are very time-consuming because of many physical parameters included. Therefore, the conventional models are not suitable in precise describing of the experimental PWVR and PWIR of FeFETs.

This paper proposes a physical model for describing polarization variation with time in a ferroelectric film and for calculating electronic device operations of FeFETs, metal-ferroelectric-metal (MFM) capacitors, and metal-ferroelectric-insulator-metal (MFIM) capacitors. In the model, the ferroelectric film can be a polycrystalline one, and to each grain, an angle θ is assigned where θ is the angle between the film normal and the direction along the spontaneous polarization. The θ distribution in the polycrystalline film is given by experiments. In fact, for SBT-based FeFETs the angle distribution was derived by an electron backscattering diffraction (EBSD) patterns technique [21].

In each grain having θ , it is also assumed that, under an electric field, a seed for polarization reversal grows along the spontaneous direction and forms a narrow column 180° reversed domain which is expanded along the sidewise direction, because 180° switching and $\pm 180^\circ$ domain formation are subjected to occur in SBT and CSBT ferroelectrics [22-24]. For $\theta \neq 0$ cases,

observations of 180° switching and 180° domain wall moving are found in [25,26].

The Kolmogorov–Avrami–Ishibashi (KAI) model [27-29] fits the physical picture mentioned above (*i.e.*, 180° domain nucleation and domain wall propagation). The KAI model provides mathematical functions of the $\theta = 0$ case describing domain expansion with time under a constant electric field. As for epitaxial thin films, many papers indicated good agreement of the KAI model with experiments [30,31], but for polycrystalline films the KAI model is asserted to be unsuitable [32]. This complicated issue concerning polycrystal films will be overcome in our present paper by introducing θ terms in grains. In order to explain wide-range $\log(t)$ distributions of polarization switching times that a Pt/Pb(Zr,Ti)O₃/Pt capacitor showed, a non-KAI model called nucleation-limited-switching (NLS) model was proposed [33]. A (111)-oriented Pb(Zr,Ti)O₃ was used. In the NLS model, the waiting times of elementary regions are stochastic. By giving exponentially broad distribution of the waiting time, the switching phenomena across a wide $\log(t)$ scale were described. Since the distribution function is assumed so that the numerical results reproduce the experimental ones, it is not easy to understand the physics. If we infer a possible inclusion of grains with other crystal orientation in the film, physics in the wide $\log(t)$ characteristics might be explained by an effect of the orientation distribution. A HfO₂-based FeFET is reported to be consistent with the NLS [34]. The paper indicates that the grain size is ≈ 20 nm and the field for creating a nucleus is ≈ 1 MV/cm. This means that the nucleation size is already the same as the grain size, and thus, there is no space left for the created nucleus to induce a wall expansion supposed in the KAI model.

Herein we propose an extended KAI (EKAI) model which is well applicable to represent characteristics of FeFETs with polycrystalline ferroelectrics under time-dependent electric field. In the EKAI model, KAI-like pictures are adopted only inside individual grains. The EKAI describes 180° switching and $\pm 180^\circ$ domain wall propagations in every grain separately. No wall motion propagates across adjacent grains are assumed. There are two fundamental premises of the EKAI. One is that only the electric field component along the spontaneous polarization works for the polarization switching. The other is that we pick up only the film-normal component of the switched polarization because the film-normal component is the important response to the externally applied potential. The in-plane components of the switching polarization are expected to be randomly distributed among grains. The effect of the in-plane components is thought to be weak because of the random distribution, and thus, the boundary conditions between neighboring grains are ignored in the present EKAI model. The polarization of the KAI model is an averaged quantity where the polarization is represented by the average of the volume fraction of $\pm 180^\circ$ domain regions. The EKAI has a distinct perspective on ferroelectrics from the phase-field model in which the ferroelectrics are divided into small segments connected by strict boundary conditions according to the idea of the LGD. The EKAI has much shorter computation time than the phase-field model because of ignoring the grain boundary conditions and averaging the ferroelectric polarizations in grains. The PWVR and

PWIR data show wide time range of polarization switching characteristics from 50 ns to 10 ms [3-6]. We suppose that these rather slow and wide-ranged time responses attribute to ferroelectric polycrystals consisting of grains which have broad distributions in the crystal-orientations. The response times of the paraelectric components in the ferroelectric grains and the dielectrics in the insulator are supposed to be much shorter than those of the polarization switching components. The potential formation time in the semiconductor is also supposed to be shorter. Therefore, the EKAI model in this paper assumes that the parameters except for the polarization switching in the ferroelectric grains varies instantaneously. Correctness of the EKAI model is supported by good agreements with experimental results of quasi-static $I_d - V_g$, $Q_m - V_g$, and PWVR for SBT-based FeFETs as discussed later in Sec. IV. The EKAI model in this paper assumes no free charges existing in the gate insulator and ferroelectric, thus the EKAI is not directly applicable to HfO₂-based FeFETs in which the ferroelectric polarization switching is always accompanied by charge injection currents [35–39].

Let us write some equations of the original KAI model, because they are necessary in the succeeding section for the EKAI derivation. In the original KAI, polarization switching nucleation is instantaneous in comparison with domain growth motion. A constant electric field and the domain wall velocity (v_{wall}) depending on this constant field are assumed. As shown in Fig. 1, the ferroelectric volume is constituted by domain regions. The switching polarizations in the downward and upward regions are P_s and $-P_s$, respectively. P_s is the spontaneous polarization. The polarization direction is parallel to the z-axis. The downward (or upward) domain regions expand with time under a positive (or negative) field, after application of step function with a constant positive field, E_{z+} . Consider a case that at the initial ($t < 0$) the volume is occupied fully by the upward regions, and a step function with a constant positive field, E_{z+} is applied at $t = 0$. Then, the volume fraction of the downward domain ($R_{dn\parallel z}$) is varied with time for $t \geq 0$ under a constant E_{z+} as:

$$R_{dn\parallel z} = c(t), \quad (1)$$

with

$$c(t) = 1 - \exp\left(-\left(\frac{t}{t_o}\right)^n\right). \quad (2)$$

t_o is the characteristic time for the polarization switching and is a function of the constant field E_{z+} . The power exponent, n , is a parameter relating to the domain growth dimension. The volume fraction of the upward domain ($R_{up\parallel z}$) is:

$$R_{up\parallel z} = 1 - c(t). \quad (3)$$

The switching polarization (\bar{P}_z) averaged over the ferroelectric volume is:

$$\bar{P}_z = R_{dn\parallel z}P_s + R_{up\parallel z}(-P_s) = P_s(2c(t) - 1). \quad (4)$$

Similarly, in the case that at the initial ($t < 0$) the volume is occupied fully by the downward regions, and step function with a constant negative field, E_{z-} is applied at $t = 0$, the volume fraction of the upward domain ($R_{up\parallel z}$) is for $t \geq 0$ under a constant E_{z-} :

$$R_{up\parallel z} = c(t). \quad (5)$$

t_o in Eq. (2) is a function of the constant field E_{z-} . The switching polarization (\bar{P}_z) averaged over the ferroelectric volume is:

$$\bar{P}_z = -P_s(2c(t) - 1). \quad (6)$$

According to Ishibashi and Takagi [29] and Ishibashi [40], in category 1, domain nucleation occurs with a fixed probability, and $n = 3$ when the wall shape is two-dimensional (*i.e.*, circular) and $n = 2$ when the wall shape is one-dimensional (*i.e.*, straight line). In category 2, there exist latent nuclei, and no new nucleation appears. In category 2, $n = 2$ when the shape is two-dimensional, and $n = 1$ when it is one dimensional. In real materials, domain nucleation may occur, and latent nuclei may also exist. Some parts are two-dimension- and others are one-dimensional-like. Hence the value n is not an integer of the range $1 \leq n \leq 3$. When t_o is small in Eq. (2), the transient time of the polarization reversal is short, when t_o is large, it is long. That is, t_o is a characteristic time that gives a time scale of the polarization variation. t_o has a relationship with v_{wall} .

For the category 1,

$$t_o = \gamma_1(v_{wall})^{(1-n)/n}. \quad (7a)$$

For the category 2,

$$t_o = \gamma_2 v_{wall}^{-1}. \quad (7b)$$

In Eq. (7), γ_1 and γ_2 are constants.

The KAI model did not show explicit mathematical forms of t_o . The wall velocity v_{wall} as a function of the applied film-normal electric field (E_z) has been investigated mainly by switching current measurement of single crystals [41,42] and by piezoresponse force microscopy (PFM) of epitaxial thin films including random disorder by defects [43–45]. A consensus view in the case of films including the disorder is that v_{wall} under high electric fields quickly increases in linear equation whereas it creeps up in reciprocal exponential at low fields [42,46]. In the case of ferroelectric films including defects, v_{wall} under high field is expressed as $v_{wall} \propto E_z$ for $E_z \gg E_{dpin}$, where E_{dpin} is a critical field over which depinning of wall motions occurs at 0 K. [46,47]. In an intermediate E_z region, v_{wall} is expressed using a power exponent τ' as,

$$v_{wall} \propto (E_z - E_{dpin})^{\tau'} \quad (8a)$$

and in a low- E_z creep region, v_{wall} is expressed at finite temperature as,

$$v_{wall} \propto \exp \left[-\frac{U'}{k_B T} \left(\frac{E_{dpin}}{E_z} \right)^\sigma \right], \quad (8b)$$

where U' is a scale of energy barrier, and σ is a power exponent originated from random disorder defects in ferroelectric films [46,47]. (k_B : the Boltzmann constant, and T : the absolute temperature).

From Eqs. (7) and (8), the v_{wall} expressions are changed to t_o expressions. Using a renormalized constant τ , Eq. (8a) is, irrespective of the category 1 or 2,

$$t_o \propto (E_z - E_{dpin})^{-\tau} \quad (9a)$$

Similarly, irrespective of the categories, Eq. (8b) is converted to t_o , using a renormalized constant U , as:

$$t_o = t_{inf} \exp \left[\frac{U}{k_B T} \left(\frac{E_{dpin}}{E_z} \right)^\sigma \right], \quad (9b)$$

where t_{inf} is a constant.

In the present work, experimental results of SBT-based FeFETs are used in order to demonstrate the EKAI model credibility. High endurance of the SBT FeFETs can be realized on small or at least moderate write-voltage conditions where the charge injection and trapping in the gate stack is suppressed [48,49]. Since a small or moderate write voltage bring a low electric field in the ferroelectric, we adopt Eq. (9b) rather than Eq. (9a) hereafter in this paper, i.e., Eq. (9b) will be used in calculations shown later. Further, since the separate determination of U and E_{dpin} is difficult, we have the following equation for t_o in this paper,

$$t_o = t_{inf} \exp \left[\left(\frac{E_{act}}{|E_z|} \right)^\sigma \right], \quad (10)$$

with an activation field constant $E_{act} (= (U/k_B T)^{-\sigma} E_{dpin})$. To include E_z negative cases, $|E_z|$ instead of E_z , is used in Eq. (10).

II. EKAI MODEL

Let us consider a ferroelectric polycrystal film as shown in Fig. 2(a). The thickness of the film is d_f . The film is divided into plural grains labeled l from one to l_{max} . All grains have the common thickness d_f . Grain boundaries are along the film normal, *i.e.*, the z -axis. The area of the grain l is A_l . The direction of the spontaneous polarization of the grain l is parallel to the u_l axis. The angle between the u_l axis and the z -axis is θ_l . The range of θ_l is defined as $0 \leq \theta_l \leq 90^\circ$. All grains have a same spontaneous polarization, P_s or $-P_s$. The polarization of the direction of the u_l axis is defined as P_s .

In Sec. IV, the EKAI model will be compared to the experimental results of MFIS FeFETs, where the ferroelectric layers consist of ferroelectric polycrystals. Experimental FeFETs with 135 nm thick ferroelectric SBT layers are available for discussion in the present EKAI model. Averaged in-plane diameters of the SBT grains are about 200nm which is larger than the ferroelectric layer thickness in the FeFETs. Therefore, we shall assume a single grain occupation along the z -direction or the film normal in the SBT FeFETs. Each grain is supposed to has a piler shape with a constant diameter from the film top to the bottom.

Figure 2(b) is an expanded schematic picture of the grain l . The grain consists of upward domain regions and downward domain regions. In the downward (or upward) domain regions, the spontaneous polarization P_s (or $-P_s$) is parallel (or anti-parallel) to the u_l axis. Figure 2(c) is a schematic picture focusing on a cylindrical-shape downward domain existing in the grain.

The EKAI model in this section describes polarization reversal behavior in one grain. The next section provides calculation schemes for the following specific devices including ferroelectric polycrystal: (1) MFM capacitors, (2) MFIM capacitors and (3) MFIS FeFETs.

1. Polarization dynamics under a time-independent electric field

In the grain l , the polarization direction is tilted from the z-axis by θ_l . However, under a constant field, E_z , the wall-motion equations are assumed to be the same as those (Eqs. (1) - (6)) of the KAI model ($\theta_l = 0$).

Consider a case that a positive constant field E_{z+} as a step function is applied at $t = 0$. At $t < 0$, the volume is occupied fully by the upward regions. Then, the volume fraction of the downward domain ($R_{dn}(l)$) is varied with time for $t \geq 0$ as:

$$R_{dn}(l) = c(t), \quad (11)$$

Remember that $c(t)$ is a function of $E_z(l)$ through t_o . The volume fraction of the upward domain ($R_{up}(l)$) is:

$$R_{up}(l) = 1 - c(t). \quad (12)$$

The switching polarization ($\bar{P}_z(l)$) averaged over the volume of the grain l is:

$$\bar{P}_z(l) = R_{dn}(l)P_s + R_{up}(l)(-P_s) = P_s(2c(t) - 1). \quad (13)$$

Consider the opposite case that a negative constant field E_{z-} as a step function is applied at $t = 0$. At $t < 0$, the volume is occupied fully by the downward regions. Then, the volume fraction of the upward domain ($R_{up}(l)$) is varied with time for $t \geq 0$ as:

$$R_{up}(l) = c(t), \quad (14)$$

The switching polarization ($\bar{P}_z(l)$) averaged over the volume of the grain l is:

$$\bar{P}_z(l) = -P_s(2c(t) - 1). \quad (15)$$

2. Effect of the spontaneous polarization direction different from the z-axis

The function $c(t)$ in Eqs. (11)-(15) is $1 - \exp(-(t/t_o)^n)$, which is the same as Eq. (2). However, the u_l axis is tilted from the z-axis by θ_l . In the EKAI model, the characteristic time for the polarization switching t_o is assumed to be

$$t_o = t_{inf} \exp \left[\left(\frac{E_{act}}{|E_z| \cos(\theta_l)} \right)^\sigma \right], \quad (16)$$

i.e., $|E_z| \cos(\theta_l)$ replaces $|E_z|$ in Eq. (10).

3. Switching polarization under time-dependent electric fields

Let us consider switching polarization evolution in the grain l in the case that the electric field varies with time. At $t = t_{now}$, it is assumed that we know the volume fraction, $(R_{dn}(l))_{now}$, of the downward domains, that, $(R_{up}(l))_{now}$, of the upward domain, the switching polarization, $(\bar{P}_z(l))_{now}$, averaged over the grain volume, and the electric field, $(E_z(l))_{now}$. $(\dots)_{now}$ means the amounts of (\dots) at $t = t_{now}$. In the following, The EKAI model provides $(R_{dn}(l))_{next}$,

$(R_{up}(l))_{next}$, and $(\bar{P}_z(l))_{next}$ at $t = t_{next}$, where $t_{next} = t_{now} + \Delta t$ (Δt : a small time-increment), and $(\dots)_{next}$ means the amounts of (\dots) at $t = t_{next}$.

The EKAI model assumes that the polarization varies during a short period Δt as if the polarization varies under a constant field $(E_z(l))_{now}$. Note, however, that we must consider two cases, *i.e.*, the cases of $(E_z(l))_{now} > 0$ and $(E_z(l))_{now} < 0$.

Figure 3 shows an explanation for the case $(E_z(l))_{now} > 0$. Let us consider a case in grain l that, at $t = t_{now}$, $R_{dn}(l)$ is $(R_{dn}(l))_{now}$ under $E_z(l) = (E_z(l))_{now}$. This status is the point A in the graph. Draw a curve of the EKAI function (Eq. (11)) at a constant field, $E_z(l) = (E_z(l))_{now}$, as the blue solid line $c(t)$ when $E_z(l) = (E_z(l))_{now}$. The line $c(t)$ has $(R_{dn}(l))_{now}$ at the point B. The time at the point B is $(t_{Kdn})_{now}$ which is obtained by solving the $c(t)$ (Eq. (2)) as

$$(t_{Kdn})_{now} = (t_o)_{now} \{-\ln[1 - (R_{dn}(l))_{now}]\}^{\frac{1}{n}} \quad (17)$$

with

$$(t_o)_{now} = t_{inf} \exp\left(\left(\frac{E_{act}}{|(E_z(l))_{now} \cos \theta_l|}\right)^\sigma\right) \quad (18)$$

We assume that the growth of $(R_{dn}(l))_{now}$ from $t = t_{now}$ to $t = t_{now} + \Delta t = t_{next}$ under $E_z(l) = (E_z(l))_{now}$ at point A is the same as the growth of $(R_{dn}(l))_{now}$ at point B under the same constant field $(E_z(l))_{now}$. The distance between the points A and B is $t_{now} - (t_{Kdn})_{now}$. The $R_{dn}(l)$ growth during Δt at the point A can thus be calculated by a parallel-shifted function, $c(t - t_{now} + (t_{Kdn})_{now})$, and thus $(R_{dn}(l))_{next}$ in the case of $(E_z(l))_{now} > 0$ is obtained as

$$(R_{dn}(l))_{next} = 1 - \exp\left(-\left(\frac{(t_{Kdn})_{now} + \Delta t}{(t_o)_{now}}\right)^n\right) \quad (19)$$

The volume fraction of the upward domain, and the z-axis component of the switching polarization averaged over the grain l are:

$$\begin{aligned} (R_{up}(l))_{next} &= 1 - (R_{dn}(l))_{next} \\ (\bar{P}_z(l))_{next} &= (R_{dn}(l))_{next} P_s \cos \theta_l + (R_{up}(l))_{next} (-P_s \cos \theta_l) \end{aligned} \quad (20)$$

$$= \left(2(R_{dn}(l))_{next} - 1\right) P_s \cos \theta_l \quad (21)$$

Quite similarly, we derive the following equations in the case of $(E_z(l))_{now} < 0$. The volume fractions of the upward domains and the downward domains are

$$(R_{up}(l))_{next} = 1 - \exp\left(-\left(\frac{(t_{Kup})_{now} + \Delta t}{(t_o)_{now}}\right)^n\right) \quad (22)$$

and

$$(R_{dn}(l))_{next} = 1 - (R_{up}(l))_{next}, \quad (23)$$

with

$$(t_{Kup})_{now} = (t_o)_{now} \left\{-\ln[1 + (R_{up}(l))_{now}]\right\}^{\frac{1}{n}} \quad (24)$$

The z-axis component of the switching polarization averaged over the grain l is:

$$(\bar{P}_z(l))_{next} = -\left(2(R_{up}(l))_{next} - 1\right) P_s \cos \theta_l. \quad (25)$$

The electric field $(E_z(l))_{next}$ can be obtained using the obtained $(\bar{P}_z(l))_{next}$ (Eq. (21) or (25))

and the electrostatic equation which depends on the device structure considered. See the next subsection. Once $(E_z(l))_{next}$ is obtained, we know now $(R_{dn}(l))_{next}$, $(R_{up}(l))_{next}$, and $(E_z(l))_{next}$. Then, the quantities of $(\dots)_{next}$ are regarded as the quantities at $t = t_{now}$ of $(\dots)_{now}$, we can repeat calculation.

When Δt is infinitesimally small, Eqs. (19) and (22) can be expressed as a differential style of $R_{dn}(l)$ and $R_{up}(l)$. That is, for $(E_z(l))_{now} > 0$

$$\left(\frac{dR_{dn}(l)}{dt}\right)_{now} = \left(1 - (R_{dn}(l))_{now}\right) \frac{n}{((t_o)_{now})^n} [(t_{Kdn})_{now}]^{n-1} \quad (26)$$

and for $(E_z(l))_{now} < 0$

$$\left(\frac{dR_{up}(l)}{dt}\right)_{now} = \left(1 - (R_{up}(l))_{now}\right) \frac{n}{((t_o)_{now})^n} [(t_{Kup})_{now}]^{n-1}. \quad (27)$$

The physical meaning of Eqs. (26) and (27) is that the differential of $c(t - t_{now} + (t_{Kdn})_{now})$ at point A in Fig. 3 equals the differential of $c(t)$ at point B.

III. TOTAL CALCULATION SCHEME FOR DESCRIBING TIME-VARING SWITCHING POLARIZATIONS OF SPECIFIC DEVICES

Figure 4 shows schematic drawing of (a) an MFM capacitor, (b) an MFIM capacitor, and (c)

an MFIS FeFET. As stated before, the ferroelectric film consists of poly-crystal grains indexed by l with $l = 1, 2, \dots, l_{max}$. We apply a time-dependent voltage, V_g , to the top metal electrode of the MFM and MFIM capacitors, and to the gate metal electrode of the MFIS FeFET. We provide the ground voltage, 0 V, to the bottom metal electrode of the MFM and MFIM capacitors, and to the semiconductor substrate terminal.

Following the EKAI model in the previous section, we derived, at a moment, the z-axis component of the switching polarization $\bar{P}_z(l)$ averaged in the volume of grain l . We assume that the paraelectric component of the ferroelectric is isotropic. The electric displacement $\bar{D}_z(l)$ averaged in the volume of grain l is represented as

$$\bar{D}_z(l) = \varepsilon_o \varepsilon_{fdi} E_z(l) + \bar{P}_z(l), \quad (28)$$

with ε_o is the permittivity in vacuum, and ε_{fdi} is the dielectric constant of the paraelectric component of the ferroelectric.

The metal electrodes of all the three devices are assumed to have large free carrier densities. At the metal electrode surfaces facing the ferroelectric or insulator, the electric-field penetrations are negligibly small, and thus no potential variations inside the metal can be assumed. The potential in the metal is uniformly V_g . Following Eq. (28) and the Gauss's law, the induced charge per unit area facing the grain l is

$$\bar{Q}(l) = \bar{D}_z(l) \quad (29)$$

Because of the averaged value of $\bar{D}_z(l)$, $\bar{Q}(l)$ is also averaged in the volume of grain l . The total induced charges of the top metal electrode of the potential, V_g , is the summation of the induced charge $\bar{Q}(l)$ over all the grains. The total induced charges are defined as the charge per unit area, Q_m , is

$$Q_m = \frac{1}{A_{tot}} \sum_{l=1}^{l_{max}} A_l \bar{Q}(l), \quad (30)$$

where A_l is the area that the grain l faces the electrode, and $A_{tot} = \sum_{l=1}^{l_{max}} A_l$. This Q_m is the quantities obtained experimentally in $Q_m - V_g$ measurements which are explained in (2) in APPENDIX. The switching polarization (*i.e.*, not including the paraelectric polarization) averaged over the entire ferroelectric, P_z , is as

$$P_z = \frac{1}{A_{tot}} \sum_{l=1}^{l_{max}} A_l \bar{P}_z(l). \quad (31)$$

Using the EKAI and electrostatic equations across MFM, MFIM, and MFIS stacks, calculation steps are expressed as follows:

1. MFM capacitor

The electrostatic equation of the MFM capacitor is

$$V_g - V_{fb} = V_f, \quad (32)$$

where V_f is the voltage across the ferroelectric layer. The flat band voltage, V_{fb} , is the work function difference between the metal top electrode and the metal bottom electrode. Since V_f does not depend on the grains, the electric field is also independent of l as

$$E_z(l) = E_z = (V_g - V_{fb})/d_f. \quad (33)$$

We have Eq. (30) as

$$Q_m = \varepsilon_o \varepsilon_{fdi} E_z + \frac{1}{A_{tot}} \sum_{l=1}^{l_{max}} A_l \bar{P}_z(l). \quad (34)$$

The second term of Eq. (34) is the switching polarization averaged over the entire ferroelectric, \bar{P}_z (Eq.(31)).

Eqs. (21) and (25) of the EKAI model in the proceeding section can give us the $\bar{P}_z(l)$ (for $l = 1 \cdots l_{max}$) at $t = t_{next}$. We also know V_g at $t = t_{next}$, because V_g is externally applied. Then, E_z and Q_m at $t = t_{next}$ are obtained by Eq. (33) and Eq. (34), respectively. We know the behavior of the MFM capacitor at $t = t_{next}$.

$R_{dn}(l)$, $R_{up}(l)$, and $E_z(l)$ at $t = t_{next}$ are regarded as those at $t = t_{now}$. The EKAI model provides $R_{dn}(l)$ and $R_{up}(l)$, and $\bar{P}_z(l)$ at $t = t_{next}$. Equation (33) gives us $E_z(l)$ at $t = t_{next}$. We repeat these procedures and obtain fully the time-dependent solution of the MFM capacitor.

2. MFIM capacitor

Charges appear at the top surface of the bottom electrode. We shall extend the z-axis-orientated boundaries between the adjacent grains into the insulator. We have the potential and E_z relationships for each grain, *i.e.*, we have the following for $l = 1, 2, \dots, l_{max}$

$$V_g - V_{fb} = V_f(l) + V_i(l), \quad (35a)$$

and

$$E_z(l) = V_f(l)/d_f. \quad (35b)$$

Here, $V_f(l)$ is the voltage across the grain l . $V_i(l)$ is the voltage across the region in the insulator belonging to the grain l . At the top surface of the bottom electrode corresponding to the grain l , the induced charge is $-Q(l)$, and we have for $l = 1, 2, \dots, l_{max}$

$$V_i(l) = \bar{Q}(l)/C_i, \quad (36a)$$

with the insulator capacitance, C_i :

$$C_i = \frac{\varepsilon_o \varepsilon_i}{d_i}, \quad (36b)$$

and

$$\bar{Q}(l) = \varepsilon_o \varepsilon_{fdi} E_z(l) + \bar{P}_z(l). \quad (37)$$

We eliminate $E_z(l)$ from Eqs. (35), (36) and (37). Then, we derive

$$\bar{Q}(l) = \frac{C_i C_{fdi}}{C_i + C_{fdi}} \left[V_g - V_{fb} + \frac{\bar{P}_z(l)}{C_{fdi}} \right], \quad (38)$$

with C_{fdi} is the paraelectric component capacitance of the ferroelectric as

$$C_{fdi} = \frac{\varepsilon_o \varepsilon_{fdi}}{d_f}. \quad (39)$$

The EKAI model provides $R_{dn}(l)$ and $R_{up}(l)$, and $\bar{P}_z(l)$ at $t = t_{next}$. We also know V_g at $t = t_{next}$, because V_g is externally applied. Equation (38) leads to $\bar{Q}(l)$ at $t = t_{next}$ for all l , and Eq. (37) gives us $E_z(l)$ at $t = t_{next}$, using the obtained $E_z(l)$ for all l . All physical quantities are

derived at $t = t_{next}$. Then similarly to the case of the MFM capacitor, we can return the EKAI model calculation, and consequently we derive the time dependent numerical solution for the MFIM capacitor.

3. MFIS FET

Figure 6 summarizes the total calculation scheme for MFIS FeFETs. Regarding the semiconductor, in the MFIS stack, the acceptor concentration (N_A) and carrier density in the semiconductor are much smaller than the carrier density in the metal layer. Thus, the electric field penetration into the semiconductor inevitably occurs so that the semiconductor surface potential ψ_s is different from the substrate potential ($V_{sub} = 0$). Imagine further a surface case where a region of an inversion state adjoins a region of an accumulation state. The surface potential cannot change abruptly on the surface. A good measure of the potential variation on the surface is the maximum depletion width, $W_m = 2\sqrt{\varepsilon_o \varepsilon_s \ln(N_A/n_i)/(e_o N_A \zeta)}$, where ε_o is the permittivity in vacuum, ε_s the relative permittivity of the semiconductor, n_i the intrinsic carrier concentration, $\zeta = e_o/(k_B T)$, and e_o the elementary charge [50]. For example, $W_m \cong 300$ nm when $N_A = 10^{16}$ cm⁻³ $T = 300$ K using $\varepsilon_s = 11.9$ and $n_i = 1.45 \times 10^{10}$ cm⁻³ for Si. If the size of ferroelectric grains is smaller than W_m , a uniform surface potential ψ_s over all the grains is a good approximation (Fig. 4 (c)). Figure 5 shows a schematic drawing of a ferroelectric-insulator-semiconductor (FIS) part of the experimental MFIS FeFETs. As shown in APPENDIX, the gate stack of the experimental FeFETs is Ir/CSBT/HfO₂/Si. Via the crystallization annealing of the CSBT, a 2.6-nm-thick SiO₂ interfacial layer (IL) was formed between HfO₂ and Si. The HfO₂ and CSBT layers are 4-nm-thick and 135-nm-thick, respectively. The bilayer of the HfO₂ and IL forms the insulator in the MFIS. Transmission electron microscope photos confirmed a thin (about 5nm-thick) transitional layer as shown in Fig. 5 (a). The transitional layer is constituted by fine grains, (≈ 5 nm) whose main elements are originated from the ferroelectric CSBT. Due to the fine sizes, these grains may be non-ferroelectric, but work as a high permittivity material. The dielectric constants of this transitional layer, the HfO₂ layer, and the SiO₂ IL are typically 180, 25, and 3.9, respectively. The different values of $\bar{P}_z(l)$ (Eq. (28)) at the bottom of the ferroelectric among the grains are averaged via the in-plane pass in the transitional layer (Fig. 5 (b)). Therefore, the switching polarization at the interface between the CSBT and the insulator consisting of the bilayer of HfO₂ and IL can be reasonably assumed to equal the z-axis component of the polarization $\bar{P}_z(l)$ averaged over all the grains, P_z , that is already defined in Eq. (31). Since P_z at the top surface of the insulator and ψ_s at the bottom of it are uniform laterally, the electric field E_i along the z-axis in the insulator and the potential V_i across the insulator are also laterally uniform, which leads to a grain-independent field E_z [$E_z(l) = E_z$ for all l] in the ferroelectric and a grain-independent potential $V_f = E_z d_f$ across the ferroelectric. The z-axis component of the electric displacement D_z averaged over all the grains as well as Q_m from Eqs. (28)-(30) are

$$Q_m = D_z = \varepsilon_o \varepsilon_{fdi} E_z + \frac{1}{A_{tot}} \sum_{l=1}^{l_{max}} A_l \bar{P}_z(l). \quad (40)$$

FeFETs have four gate-, source-, drain-, and substrate-terminals. Let us consider the case where the gate voltage V_g is generally varied with time and other terminals are grounded ($V_s = V_d = V_{sub} = 0$). Here V_s , V_d , and V_{sub} are the voltages applied on the source, drain, and substrate, respectively. The electrostatic equation across the MFIS stack is,

$$V_g - V_{fb} = V_f + V_i + \psi_s, \quad (41)$$

where V_{fb} is the flat-band voltage, *i.e.*, difference between the metal work function and semiconductor fermi level. By eliminating E_z from Eqs. (40) and (41) and using the Gauss's law with noticing the capacitance definition of Eqs. (36b) and (39), we have

$$V_g - V_{fb} + \frac{1}{A_{tot}} \sum_{l=1}^{l_{max}} A_l \bar{P}_z(l) = Q_m \left(\frac{1}{C_f} + \frac{1}{C_i} \right) + \psi_s. \quad (42)$$

If there is no interface state density between the insulator and semiconductor, the induced charge density, Q_s , in the semiconductor surface region has the same magnitude as Q_m with the opposite polarity ($Q_m = -Q_s$). The Q_s is a function of semiconductor surface potential ψ_s as follows [50],

$$Q_s = \mathcal{F}(\psi_s) = \mp \frac{\sqrt{2\varepsilon_o\varepsilon_s}}{\zeta L_D} \left[e^{-\zeta\psi_s} + \zeta\psi_s - 1 + \frac{n_{po}}{p_{po}} (e^{\zeta\psi_s} - \zeta\psi_s - 1) \right]^{\frac{1}{2}}, \quad (43)$$

with negative sign for $\psi_s > 0$. This equation is for n -channel FeFETs formed in p -type substrates. The equation for p -channel FeFETs can be rewritten appropriately. The Debye length is $L_D = \sqrt{\varepsilon_o\varepsilon_s/e_o p_{po} \zeta}$ with $p_{po} = (N_A - N_D + ((N_A - N_D)^2 + 4n_i^2)^{1/2})/2$ and $n_{po} = n_i^2/N_A$. The donor-, acceptor-, and intrinsic-carrier-densities in the semiconductor are N_D , N_A , and n_i , respectively, and p_{po} and n_{po} are the equilibrium densities of holes and electrons, respectively.

In the case that the interface states between the semiconductor and insulator are considered, the equation $Q_m = -Q_s$ is modified as

$$Q_m = -Q_s - Q_{it}, \quad (44)$$

where Q_{it} is the trapped charge at the interface per area that is expressed as

$$Q_{it} = -e_o \int N_{it}(\mathcal{E}) F_{SA}(\mathcal{E} - e_o\psi_s) d\mathcal{E}. \quad (45)$$

Here, \mathcal{E} is an electron-energy variable, $N_{it}(\mathcal{E})$ is the area density of interface-states per electron energy, and F_{SA} is the Fermi-Dirac distribution function for acceptors [50].

In the case that $N_{it}(\mathcal{E})$ is approximated as a constant D_{it} [$V^{-1}cm^{-2}$] with respect to the energy, Q_{it} can be approximated as

$$Q_{it} = -e_o D_{it} \psi_s. \quad (46)$$

For convenience of numerical root-finding calculations, we emphasize that Q_s (Eq. (43)) monotonically decreases with the increase of ψ_s , and Q_{it} (Eq. (45) or (46)) also has the same monotonical property. Equation (44) shows that Q_m is a monotonically increasing function of ψ_s .

See Eq. (42). The right-hand side quantity is a monotonically increasing function of ψ_s . At $t = t_{next}$ in the previous section, we derived $\bar{P}_z(l)$ for all l by either Eq. (21) or (25). V_g at $t = t_{next}$ is given by an external voltage source. Thus, the left-hand side of Eq. (42) is a known constant at $t = t_{next}$. The right-hand side of Eq. (42) consists of only one variable ψ_s and is a

monotonically increasing function of ψ_s . Hence, ψ_s can be uniquely determined at $t = t_{next}$. Once ψ_s is determined, we derive Q_m from Eqs. (43) – (46), and E_z from Eq. (40) at $t = t_{next}$.

We now have E_z at $t = t_{next}$, and, in the previous section, have $R_{dn}(l)$ and $R_{up}(l)$ at $t = t_{next}$ for all l . The set of E_z , $R_{dn}(l)$, and $R_{up}(l)$ at $t = t_{next}$ replaces a set of E_z , $R_{dn}(l)$, and $R_{up}(l)$ at $t = t_{now}$. If $E_z > 0$, $R_{dn}(l)$ and $R_{up}(l)$ at $t = t_{next}$ are obtained by Eqs. (19) and (20). If $E_z < 0$, $R_{up}(l)$ and $R_{dn}(l)$ at $t = t_{next}$ are obtained by Eqs. (22) and (23). The procedure of this section gives us E_z at $t = t_{next}$. Repeating these procedures provide dynamics of the MFIS FeFETs.

The status of the polarization in ferroelectric or the electric displacement can be monitored by the drain current, I_d , of the sub-threshold region, which is represented as functions of the drain voltage V_d and the surface potential ψ_s by [50]

$$I_d = \frac{\mu k_B T}{e_0} \sqrt{\frac{\epsilon_0 \epsilon_s p p_0 k_B T}{2}} \left(\frac{n_i}{N_A}\right)^2 (1 - e^{-\zeta V_d}) e^{\zeta \psi_s} (\zeta \psi_s)^{-1/2}. \quad (47)$$

In this paper, all numerical results of FeFETs are obtained on the premise of $V_s = V_d = V_{sub} = 0$, whereas the practical I_d measurements of n -channel FeFETs are usually on the condition of $V_d = 0.1$ V and $V_s = V_{sub} = 0$. Such a small difference in V_d condition does not affect the validity of comparing results from the calculations and the measurements.

The EKAI, the formulae from Eq. (11) to Eq. (27), and the total calculation scheme for MFIS FeFETs, those from Eqs. (28) to (31) and from Eqs. (40) to (47), describe the general transient response of MFIS FeFETs under time-dependent V_g conditions. The formulae also cover slowly changing phenomena. There is so-called data retention mode, in which all the quantities such as Q_m , E_z , $R_{dn}(l)$, and $R_{up}(l)$ vary very slowly, and the Δt values in Eqs. (19) and (22) can be chosen flexibly with minimal changes of those quantities; thus, retention results of the period of days and years are obtained in a practical computation time.

IV. CALCULATION RESULTS OF FEFETS AND COMPARISON TO THE EXPERIMENTAL

The EKAI model and the total calculation scheme of this paper is verified using experimental data of FeFETs consisting of MFIS gate stacks of Ir/CSBT/HfO₂/IL/Si. The experimental details were reviewed in APPENDIX. An insulator (I) in the modeled MFIS FeFET corresponds to the bilayer of IL and HfO₂ in a real CSBT FeFET. Capacitance of the I (C_i) was evaluated as $C_i = 0.99$ $\mu\text{F}/\text{cm}^2$. Regarding ferroelectric (F), dielectric constant ϵ_{fdi} of the paraelectric component is determined by the $Q_m - V_g$ curves at $V_g < 0$ or in the third quadrant of Fig. A2 because the semiconductor depletion layer does not affect at $V_g < 0$. In the third quadrant, by taking the gradient of the curve of a V_g sweep amplitude, the combined capacitance of C_i and C_{fdi} (Eqs. (36b) and (39)) was 0.54 $\mu\text{F}/\text{cm}^2$. Since $C_i = 0.99$ $\mu\text{F}/\text{cm}^2$ and $d_f = 135$ nm, $\epsilon_{fdi} = 180$ at room temperature was obtained and used for calculation in the EKAI. The P_s direction of SBT and CSBT

ferroelectrics is the a -axis direction of the crystal unit cell of SBT and CSBT [51, 52].

With regard to the angle θ_l and the area A_l , The technique of EBSD patterns could characterize the crystal orientation and grain size. The bar-graph plots in Fig. 7 show the distribution function of grains with the orientation angle θ . The quantity of the vertical axis is the area of grains whose θ is in the range from θ to $\theta + \Delta\theta$ ($\Delta\theta$: the bar width). The scanning area of EBSD, $\approx 56 \mu\text{m}^2$, is not enough for statistical treatment, meaning that ΔV_{th} versus $\log(t_w)$ curves simulated by the EKAI model and the calculation scheme using the bare bar-graph plots were not smooth. As shown in Fig. A4, the experimental $\Delta V_{th} - \log(t_w)$ curves are very smooth. Therefore, we used a fitted smooth curve in Fig. 7 instead of the bare data. Although the smoothed curve is used in the actual calculation, the curve is digitized at every 3° to save calculation time.

When we make quasi-static calculation of $I_d - V_g$ and $Q_m - V_g$, a sinusoidal V_g function is provided as $V_g = V_{fb} + V_{amp} \sin(2\pi f_s t)$. The frequency f_s and the calculation time-length are typically set as 10 Hz and 0.2 s, respectively. The time step $\Delta t = 1 \times 10^{-9}$ s is commonly used in the calculation of $I_d - V_g$, $Q_m - V_g$, and PWVR. Validity of the value Δt and accuracy of the calculated results were verified by confirming that calculations with $\Delta t = 0.5 \times 10^{-9}$ s gave the same results as those with $\Delta t = 1 \times 10^{-9}$ s.

Experimental $I_d - V_g$ curves do not suggest any electron-energy dependence of $N_{it}(\mathcal{E})$ in Eq. (45), and thus we use D_{it} and Eq. (46) regarding the interface states between the insulator and semiconductor. Several series of $I_d - V_g$ simulations with various V_{fb} and D_{it} values were examined and compared to the experimentally obtained $I_d - V_g$. We found that $D_{it} = 4 \times 10^{12} \text{ V}^{-1} \text{cm}^{-2}$ is a good value to fit the experiment. Regarding V_{fb} , the suitable range was between -0.8 V and -1.0 V, so we used $V_{fb} = -0.8 \text{ V}$ in this work.

The exponent σ of v_{wall} in Eq. (8b) and of t_o in Eqs. (9b) and (10) is generally $\sigma \neq 1$ according to the PFM experiments and the analyses by phenomenological theories of random disorder potentials generated by imperfections in epitaxial films. The magnitude of σ depends on materials and the material preparation methods [53]. Some experiments indicated $\sigma \approx 0.5$ of BaTiO₃ [54], 0.5 – 0.6 in PbZr_xTi_{1-x}O₃ (PZT) of $x = 0.2$ [55], and 0.20 – 0.28 of ferroelectric organic polymer [56]. A report of a PZT showed the σ decreased with raising defect densities intentionally [44]. Studies on epitaxial PZT films indicated $\sigma \approx 0.9$ and ≈ 1.0 [43,46]. Regarding single crystals, those of BaTiO₃ and triglycine sulfate suggested the switching currents follow exponential functions without introducing decimal exponents [41,42]. In an early theoretical work on the wall propagation in a single crystal without disorders by Miller and Weinreich [57], v_{wall} in a BaTiO₃ single crystal was expressed by an exponential form equivalent to Eq. (8b) when $\sigma=1$. Among other subsequent discussions whether a practical σ should equal one or not, a theoretical work by atomistic molecular dynamics simulation supported the validity of $\sigma=1$ [58]. Zhao et al. [59] showed that polarization switching times of ferroelectric organic polymer films obeyed simply the Merz exponential law [41]. We did not use a method for intentionally introducing defects during annealing processes for ferroelectric layer crystallization of MFIS

FeFETs. Like these, there is no reason to adopt σ of much less than 1. In the following simulation, we thus assume $\sigma = 1$.

We adopt $n = 1.3$ in the function $c(t)$ that is a value reported for an epitaxial PZT film under less electric field than 200 kV/cm [31]. It is also close to another n for polymer ferroelectric films with a range from 1.0 to 1.5 [59]. The n corresponds to the dimension of the domain shape. The calculated results were insensitive to the varying n from 1 to 3. We use acceptor density $N_A = 1 \times 10^{16} \text{ cm}^{-2}$ whose fluctuation does not affect the calculated results very much.

The remaining parameters, E_{act} , t_{inf} , and P_s can be determined by curve fitting of numerical results to the experimental about the ΔV_{th} vs. t_w in PWVR. The experimental results of ΔV_{th} vs. t_w are found in Fig. A4 in APPENDIX. Regarding the numerical results, PWVR simulations with varying E_{act} , t_{inf} , and P_s are introduced in Figs. 8 (a), (b) and (c), respectively. Every marker corresponds to a calculated point of ΔV_{th} vs. t_w . Using the cases of Fig. 8, we show how uniquely three parameters, E_{act} , t_{inf} , and P_s , are determined. We present a reference curve (the blue solid line with filled square markers in Fig. 8(a), (b), and (c), respectively), which was a numerical solution for well simulating an experimentally obtained ΔV_{th} vs. t_w . The reference curve was drawn using a set of parameters $E_{act} = E_o$, $t_{inf} = t_1$, and $P_s = P_o$ with $V_h = -V_l = 4 \text{ V}$. The E_o , t_1 , and P_o are constants for the sake of explanation. The E_{act} and t_{inf} are deeply involved in ferroelectric polarization dynamics. The P_s is an inherent parameter of the ferroelectric. As shown in Fig. 8(a), if E_{act} is as large as $1.7 E_o$, the increase of ΔV_{th} with t_w is very slow, and the curve is far from the reference curve in a realistic t_w range of the experimental. If E_{act} is as small as $0.43 E_o$, rapidly increasing ΔV_{th} approaches a saturated value. This is far from the log-linear styles. An appropriate ΔV_{th} can draw a log-linear curve like the reference curve at $E_{act} = E_o$. As shown in Fig. 8(b), t_{inf} determines a quantity of the ΔV_{th} vs. $\log(t_w)$ curve shift in parallel along the $\log(t_w)$ axis. The polarization growth in Eqs. (21) or (25) is proportional to P_s , meaning that if P_s is larger, the separation between a ΔV_{th} vs. $\log(t_w)$ curve written by pulses of $V_h (= -V_l)$ and the neighboring curve written by $V_h \pm 1V (= -V_l \mp 1V)$ is wider. See Fig. 8(c), where the curves are drawn in the case of $P_s = P_o$ and $1.7P_o$, respectively. The role of P_s is to adjust this separation distance to fit the experimental results. By experiencing these processes, E_{act} , t_{inf} , and P_s are uniquely determined under a fixed σ . Here, “uniquely determined” means that no solutions having a new parameter set exist far from the derived parameter set.

Remember that E_{act} has a meaning of an activation- or a threshold-field for domain wall motions as Eqs. (9b) and (10) indicate. The domain wall energy is affected by elastic and electric-dipole contributions in atomic scales. Theoretical works [44,57,60,61] indicated that the domain wall energy included a power exponent of P_s , indicating that the E_{act} may also be a function of P_s . Since the treated temperature is only room temperature, three parameters P_s , E_{act} and t_{inf} can be searched independently to fit the experimental data. In the case that temperature is varied, P_s is also changed with temperature. We must consider that E_{act} is a function of P_s via the domain wall energy in addition to the thermally-activation term $(k_B T)^{-1}$ (Eq. (9b)).

Figure 9 shows a fitting result of PWVR where the calculated curves compared to the experimental data at $V_h = 3$ V, 4 V, 5 V, and 6 V. Markers represent the calculated points of ΔV_{th} vs. t_w using an optimum parameter set of $E_{act} = 828$ kV/cm, $t_{inf} = 8.30 \times 10^{-12}$ s, and $P_s = 3.0$ $\mu\text{C}/\text{cm}^2$. Solid lines mean the experimental results of Fig. A4 introduced in APPENDIX. The calculation well simulated the experimental ΔV_{th} vs. $\log(t_w)$ throughout the wide t_w range from 50ns to 0.5 ms. Other parameters for the calculation are summarized as follows: $\sigma = 1$, $n = 1.3$, $V_{fb} = -0.8$ V, $D_{it} = 4 \times 10^{12}$ $\text{V}^{-1}\text{cm}^{-2}$, $N_A = 1 \times 10^{16}/\text{cm}^3$, $d_f = 135$ nm, $\varepsilon_{fdi} = 180$, $d_i = 3.5$ nm, and $\varepsilon_i = 3.9$.

Using the same values of parameters as those solved for fitting PWVR (Fig. 9), other correlations were simulated which were quasi-static characteristics of $I_d - V_g$ (Fig. 10) and $Q_m - V_g$ (Fig. 11) with various V_g sweep amplitude. The calculated results are drawn with thick and red-colored lines. The experimental are expressed by thin lines colored in black. In the calculations, V_{th} was defined as V_g at which the semiconductor surface potential ψ_s was equal to 85% of $2\psi_B$, the surface strong inversion condition. (*i.e.*, $\psi_s = 2\psi_B \times 0.85$ where $\psi_B = (1/\zeta)\ln(N_A/n_i)$ [50]). Figures 10 and 11 show moderate agreements of the calculated results with the experimental. However, high curvature of $Q_m - V_g$ around $V_g = 0$ V seems more emphasized in the calculated than in the experimental as shown in Fig.11. As an effort of the $Q_m - V_g$ matching, for example, D_{it} may be raised for decreasing the nonlinearity of $Q_m - V_g$. But the attempt enhances another mismatch in $I_d - V_g$ as shown in Fig. 10. Reason of the inconsistency is not clear now. Despite having some numerical mismatch remained in the curve fitting, the EKAI model and the calculation scheme qualitatively and comprehensively well simulate FeFET characteristics such as dynamic PWVR and quasi-static $I_d - V_g$, and $Q_m - V_g$

V. DISCUSSION

A. Q_m versus E_z correlations in PWVR of the EKAI

In the EKAI model, a Q_m vs. E_z correlation is calculated along a hysteresis loop as shown in Fig. 12(a). The drawing sequence is explained by corresponding V_g variations with checkpoints as shown in Fig. 12(b), which are, **a'**, **b**, **c**, **d**, **g**, **g'**, **d'**, **e**, **f**, **a**, **h**, **h'** and back to **a'**, repeated cyclically in this order. A positive pulse writing (PPW) is simulated passing through **a'**, **b**, **c**, and **d**. A negative pulse writing (NPW) is simulated passing through **d'**, **e**, **f**, and **a**. As stated in the introduction, we assume in this paper that the parameters except for the polarization switching varies instantaneously. In four segments on the $Q_m - E_z$ curve, points instantaneously move from **a'** to **b**, from **c** to **d**, from **d'** to **e**, and from **f** to **a**. These curves can be written as

$$Q_m = \varepsilon_o \varepsilon_{fdi} E_z + P_{zconst}, \quad (48)$$

where P_{zconst} is a constant that each straight line has, and P_{zconst} equals P_{zb} , P_{zc} , P_{ze} , and P_{zf} for

the line **a'-b**, **c-d**, **d'-e**, **f-a**, respectively.

Initially, idling write cycles are executed which consist of PPW and NPW without a V_{th} reading (VR). The idling cycles have the role to make the $Q_m - E_z$ trajectory converged into the steady loop shown in Fig. 12(a). The simulation can be started from the coordinate origin at $t = 0$, where $E_z = 0$, $Q_m = 0$, and $R_{dn}(l) = R_{up}(l) = 1/2$ for all l . The $Q_m - E_z$ trajectory changes during the idling write cycles and soon become converged after experiencing plural cycles. Then the PWVR operation starts. After one PPW is executed, a VR is simulated passing through **d**, **g**, **g'**, **d'**. After one NPW is executed, another VR is simulated passing through **a**, **h**, **h'**, **a'**. Up to the turnaround points **g'** and **h'**, quasi-static read operations are performed after PPW and after NPW, respectively. At a reference level of Q_m , *i.e.*, at points **g** and **h**, V_{th} values are decided. At read, V_g is swept to V_{swp_end} (*i.e.*, V_g at point **g'** and **h'**).

As discussed in III. 3, the electrostatic potential equation across the MFIS stack (Eq. (41)) is valid at any moment where $V_f = E_z d_f$ and $V_i = Q_m / C_i$. The Q_m is a function of ψ_s by a discussion at Eqs. (43)-(46). Consequently, at any time, $Q_m - E_z$ satisfies the rule of the following:

$$Q_m = -C_i d_f (E_z - (V_g - V_{fb} - \psi_s) / d_f) \quad (49)$$

Curves described by Eq. (49) is called a load line in this paper. Four load lines I, II, III, and IV appear in Fig. 12(a). The load lines I, II, III, and IV are the lines when V_g in Eq. (49) equals V_h , 0, V_l , and V_{swp_end} , respectively. Equation (49) indicates that a solution point (E_z, Q_m) locates at any moment (t_a) on a load line having the V_g value at $t = t_a$. The EKAI model decides which point on the load line is really the solution point.

The point **b**, **d**, **g**, and **a** are decided by that Eq. (48) and Eq. (49) are simultaneously satisfied. From **b** to **c** in PPW, the EKAI model describes a P_z increase from P_{zb} to P_{zc} during the period t_{w1} of V_h application (Eq. (19)). Similarly, from **e** to **f** in NPW, the model describes a P_z decrease from P_{ze} to P_{zf} during the period t_{w2} of V_l application (Eq.(22)).

In the period **d-g-g'-d'** and **a-h-h'-a'**, V_{th} read operations are performed. V_g is swept from 0 V to V_{swp_end} . When $V_g = V_{swp_end}$, **g'** and **h'** are also on the load line IV. As stated, V_{th} values are decided at a reference level of Q_m , *i.e.*, at points **g** and **h**. As also stated, Q_m and ψ_s have a single-valued function relationship each other. The reference level of ψ_s (ψ_{th}) can replace the reference of Q_m . The ψ_{th} is chosen in a sub-threshold region of the FeFETs so that $\psi_B \leq \psi_{th} \leq 2\psi_B$. The EKAI model indicates that, during a V_g sweeping after NPW, there is a tendency that P_z increases. If this is visible, the point **a'** separates from **a** and shifts to the E_z smaller direction on the load line II. The EKAI model works during the period **d-g-g'-d'** and **a-h-h'-a'**. This period is in a data-retention stage even though no read operation is done. If the depolarization electric field is not small, Q_m shifts to the $|Q_m|$ decreasing direction on the load line II. In this sense, **d'** and **a'** differ from **d** and **a**, respectively. The decrease amounts depend on the relationship among E_{act} , E_z , and $\cos(\theta_l)$, as shown in Eq. (16).

Note that, in drawing the loop in Fig. 12(a), it passes through two points: the maximum

induced charge (Q_{mmax}) and the minimum one (Q_{mmin}) (*i.e.*, the negative maximum one). The Q_{mmax} and $-Q_{mmin}$ decide the amount of an undesirable current of the direct tunneling type or the electric-field-assisted (Fowler-Norheim, FN) tunneling type. At $Q_m = Q_{mmax} = Q_{mmin}$, $|V_{imax}| = Q_{mmax}/C_i = -Q_{mmin}/C_i$ is defined where the V_{imax} is the maximum voltage drop across the insulator. If $Q_{mmax} = 2.0 \mu\text{C}/\text{cm}^2$ and the insulator is 1.6-nm-thick SiO_2 , then $V_{imax} = 0.93 \text{ V}$ and the corresponding field maximum of the insulator, $E_{imax} = 5.8 \text{ MV}/\text{cm}$. Let us estimate gate leakage currents thorough the insulator. Using a high permittivity insulator or a combination of such insulators weakens the field a little, but the field is still high enough to induce the leakage currents. Investigations of the tunneling current of polysilicon/ SiO_2 /Si [62,63] are good references to know the impact of the charge injection for the MFIS stacks where the semiconductor is Si. The charge injection is mainly caused by the tunneling current through the IL (*i.e.*, SiO_2). We propose a significant guideline in investigating ferroelectric FETs. Imagin what happens at $Q_m = Q_{mmax} = 2.0 \mu\text{C}/\text{cm}^2$. At this moment, the charge injection is the highest. According to Ref. 62, in the case that SiO_2 was about 1.6nm thick, the tunneling current was $\approx 10 \text{ A}/\text{cm}^2$ at the 5.8 MV/cm whereas it was $\approx 10^{-5} \text{ A}/\text{cm}^2$ in the case of about 3.2 nm thick SiO_2 , at the same field. The voltage drops across the SiO_2 layer, Q_m/C_{SiO_2} , [C_{SiO_2} : the SiO_2 layer capacitance] at $Q_m = 2.0 \mu\text{C}/\text{cm}^2$ are 0.93 V and 1.85V for the 1.6 nm thick and 3.2nm thick SiO_2 layers, respectively. By choosing this twice thick insulator SiO_2 , the tunneling current decreases $\approx 10^{-6}$ times, and the V_g for writing increases only about 0.9 V. As this quantitative consideration indicates, there seems no way to avoid the tunneling current except for increasing the thickness for SiO_2 . The same story is valid in MFIS. For preserving the nonvolatile device reliabilities, the IL SiO_2 should be moderately thick enough to avoid charge injection caused by the tunneling current. A strategy of thinning SiO_2 is logically failed.

If charge injections are not negligible, a scenario is as follows: In PPW, electrons are injected from the silicon. The electrons may mostly arrive at the metal electrode and be absorbed. However, some of them are trapped in the ferroelectric layer, the insulator, and the interface between the ferroelectric and insulator. The trapped ones near the silicon side may return to the semiconductor by tunneling back after PPW [37], but other trapped electrons remain trapped, leading to the increase of V_{th} of n -channel FeFETs. While NPW holes are injected from the silicon. Similarly, some holes are stably trapped, leading to the decrease of V_{th} of n -channel FeFETs. Since the number of trapped electrons after PPW and that of trapped holes after NPW are not the same, unintended V_{th} shifts appear with increasing the cycle of PPW and NPW in endurance tests.

On the load lines I, II, III, and IV mentioned above, P_z - and Q_m -increase accompanies E_z decrease, meaning that a capacitance dQ_m/dE_z is negative. Note that, as described in the EKAI model and the total calculation scheme, the time response of the linear dielectric part is instantaneous, but P_z variation needs time. Thus, while V_g is swept back and forth between negative and positive voltages, the derived $Q_m - V_g$ and $I_d - V_g$ curves inevitably draw hysteresis loops. The EKAI model does not realize the idea discussed in Ref. 64 regarding steep-slope non-

hysteresis transistors during on-off operation for back-and-forth voltage sweeping.

B. Coercive field in the EKAI model

Although the coercive fields can be read in the $Q_m - V_g$ hysteresis curves derived by the calculation of this model, the EKAI model of this paper does not contain the coercive field (E_c^*) as an explicit parameter. Let us find the relationship between the model and E_c^* for a case of a single grain ferroelectric indexed by θ . To take Q_m vs. E_z curves, a triangular shape E_z as a function of time, like Fig. 13(b), whose linear slope is K , is supplied to an MFM capacitor. Fig. 13(a) shows a P_z vs. E_z curve. During E_z increasing with time, R_{dn} varies from 0 to 1, like Fig. 13(c). Since $E_z = K \cdot \text{time} + \text{constant}$, R_{dn} vs. time is converted to R_{dn} vs. E_z . At a narrow region of E_z , R_{dn} increases rapidly, as shown in Fig. 13(c). The R_{dn} rapid increase corresponds to P_z increase of the right-side branch of the hysteretic loop in Fig. 13(a), indicating that an E_z at which the R_{dn} rapid increase occurs is regarded as a coercive field. Since the R_{dn} increase is rapid within a narrow range of E_z , a defined coercive field well approximates E_c^* which is defined as the field at $Q_m = 0$ (Fig. 13(a)). The E_z representing this narrow range field can be decided by the E_z (E_{cm}) at which dP_{dn}/dE_z takes a maximum (Fig. 13(d)). E_{cm} is the coercive field derived analytically in the EKAI model. Exactly speaking, E_{cm} approximates E_c^* , but E_{cm} is not equal to E_c^* .

By starting from Eq. (26) with use of $dE_z = Kdt$ and by calculating the second derivative, $d^2R_{dn}/dE_z^2 = 0$, we have, without any approximation,

$$\exp\left[-\left(\frac{E_{act}}{E_z \cos\theta}\right)^\sigma\right] - \frac{\sigma K \cos\theta}{E_{act}} \frac{t_{inf}}{g(n)} \left(\frac{E_{act}}{E_z \cos\theta}\right)^{\sigma+1} = 0 \quad (50)$$

with $g(n) = n[-\ln(1 - R_{dn})]^{(n-1)/n} - (n-1)[- \ln(1 - R_{dn})]^{-1/n}$.

In Eq. (50), K is the sweep slope, and E_{act} , t_{inf} and σ are the model simulation parameters. In $g(n)$, n is the model parameters. Although $g(n)$ contains R_{dn} , $g(n)$ weakly depends on R_{dn} variation. This means $g(n)$ can be regarded as a constant. (In the case of $n = 1$, $g(n)$ equals 1, and Eq. (50) does not contain the dimension parameter, n .) Hence, Eq. (50) can be solved for E_z , and the root of it is E_{cm} .

Equation (50) is a finding-root problem of $x_e = E_{act}/E_z \cos\theta$ on the condition of $g(n)=1$. Since E_{act} is included in x_e , E_{cm} is changed rapidly with E_{act} . Since K appears only in the coefficient in Eq. (50), the coercive field E_{cm} varies slowly with K . The solid curve is the solution of Eq. (50), where K is varied with the constants of $\sigma = 1$, $E_{act} = 828$ kV/cm, and $t_{inf} = 8.30 \times 10^{-12}$ s. The filled-circle markers are the results of the full simulation of the EKAI model with MFM capacitor structures. Good agreement is confirmed between the solid line and the filled circles. The obtained E_{cm} values that vary with K are about 50 kV/cm. This value agrees well with the experimentally known value of SBT. In fact, the $Q_m - V_g$ curve of an MFM with a (100)/(010)-oriented SBT thin film [65] showed $E_c^* = 48$ kV/cm when the swing amplitude and

frequency were 225 kV/cm and 20Hz that corresponds to $K = 1.8 \times 10^4$ (kV/cm)/s. This point is added in the inset graph of Fig. 13(e) as the filled square, indicating good agreement with the solid curve by Eq. (50).

Slower sweeping cases are also solved by Eq. (50) as shown in the solid curve of Fig. 13 (e). E_{cm} decreases very slowly with the decrease of $\log(K)$. The figure shows $E_{cm} = 48$ kV/cm and 20 kV/cm at $K = 1.8 \times 10^4$ (kV/cm)/s and 5.5×10^{-8} (kV/cm)/s, respectively. This means that E_{cm} is 20 kV/cm when the field is swept with a cycle period of 1.6×10^{10} s (≈ 500 years) with sweeping ± 225 kV/cm. That is to say, although the model does not have a coercive field as an explicit parameter, the derived results assure nonvolatile performance.

VI. CONCLUSION

An extended KAI (EKAI) model for describing the electrical properties of ferroelectric-gate field effect transistors was proposed. The model is physics-based and was validated via comparison with rich experimental data of metal-ferroelectric-insulator-semiconductor type FeFETs where the ferroelectrics were of SBT or CSBT Bi-layered-perovskite oxides. The model features and the results of comparison with the experimental data are summarized as follows.

(The EKAI model and the calculation scheme for FeFETs)

The orientation angle θ of each grain in the ferroelectric film and its size is assigned, where θ is the angle between the film normal and the spontaneous polarization direction. In each grain, polarization reversed domain nucleation occurs along the spontaneous polarization direction, and the domain wall expands to the lateral direction of the P_s direction. In the case of large θ , the time scale of transient phenomena under an electric field is much larger than that in the $\theta = 0$ case. This is the essential cause that the ΔV_{th} vs. t_w of PWVR indicates log-linear relationships.

Since the ferroelectric thickness of experimental FeFETs compared to the model is 135 nm, which is comparable with the average size of grains, we assumed a single grain occupation along the z -direction in the SBT FeFETs. Each grain is supposed to have a pillar shape with a constant area from the film top to the bottom.

The electrostatic condition of the MFIS stacked structure renders a time-varying electric field in each grain in the ferroelectric film. The KAI equation about the time evolution of polarization is presented on a condition of a fixed electric field. The EKAI model represents polarization variation under the time-varying field as follows: At $t = t_{now}$, let grain l have the volume fraction of the downward polarization domain $(R_{dn}(l))_{now}$ at a positive field $(E_z)_{now}$. The polarization changes from t_{now} to $t_{next} = t_{now} + \Delta t$ as if the $(R_{dn}(l))_{now}$ would change under a constant $(E_z)_{now}$. In the case of negative $(E_z)_{now}$, the volume fraction variation of the downward domain $(R_{up}(l))_{now}$ is calculated similarly. At $t = t_{next}$, using obtained $(R_{dn}(l))_{next}$ or $(R_{dn}(l))_{next}$ and

the external gate voltage, the electrostatic equations of MFIS stack derives the electric field $(E_z)_{next}$. By repeating this procedure from t_{now} to t_{next} , the time-dependent behavior of FeFETs can be derived.

The characteristic time $t_o \propto \exp(\text{const.}/E_z \cos\theta)$ in the EKAI model is a measure of switching time of respective grains. Wide distribution of θ makes the time FeFET response quite broad on the $\log(t)$ scale. Regarding the connection of the ferroelectric to the insulator and semiconductor, the polarization is averaged over the area at the bottom of the ferroelectric film. This average procedure can be accepted because semiconductors have a much smaller ability to shield polarization than metals and the transitional layer at the bottom of the ferroelectric works for averaging the polarization variation among the grains.

(Comparison with experimental data and discussion)

The parameters, P_s , E_{act} , and t_{inf} can be uniquely determined in comparison with experimental data as $P_s = 3 \mu\text{C}/\text{cm}^2$, $E_{act} = 828 \text{ kV}/\text{cm}$, $t_{inf} = 8.30 \times 10^{-12} \text{ s}$. Using these parameters, I_d vs. V_g , Q_m vs. V_g , and PWVR were calculated. The calculation results were explained consistently and entirely the corresponding experimental data.

Transient behavior can well be understood using Q_m vs. E_z planes. The paraelectric component in $Q_m (= D_z)$ of Eq. (40) instantaneously follows the electric field variation $Q_m = \epsilon_o \epsilon_{fdi} E_z + P_{zconst}$ (Eq. (48)). Q_m always moves on the load line $Q_m = -C_i d_f (E_z - (V_g - V_{fb} - \psi_s)/d_f)$. On the PWVR measurement, V_g is set to equal V_h or V_l , at the pulse write (PW) stage and is swept in a small voltage range to find the V_{th} at the V_{th} read (VR) stage. At the PW stages, P_z and Q_m grow via the EKAI model during the pulse width t_w and finally reaches the maximum or the negative maximum of Q_m .

In order to suppress the effect of charge trapping in the FeFET operations, there should be restrictions on the values of Q_{mmax} and $-Q_{mmin}$. The guideline was proposed for avoiding the charge injection. For preserving the nonvolatile reliabilities, the IL SiO_2 should be moderately thick enough to avoid charge injection caused by the tunneling current.

On the load line mentioned above, the increase in P_z and Q_m accompanies the decrease in E_z , meaning that a capacitance dP_z/dE_z is negative. In our model, linear dielectric response is instantaneous, but P_z variation needs time, and thus, during back-and-forth sweeping of V_g , the derived curves of $Q_m - V_g$ and $I_d - V_g$ always draw hysteresis loops.

The EKAI model and the calculation scheme do not explicitly have a coercive electric field (E_c^*). When a triangular waveform field is given across the ferroelectric film for a metal-ferroelectric-metal capacitor, a simple equation (Eq. (50)) is derived, containing the field increasing rate, K , as well as E_{act} , and t_{inf} . The root of Eq. (50) gives an electric field E_{cm} that approximates E_c^* . E_{cm} decreases with the decrease of K , but even if a very slow K corresponding to a time scale of more than 100 years is chosen, a sufficient E_{cm} remains. This means that the EKAI model assures a non-volatile memory function which the ferroelectrics hold.

The EKAI model of this paper described polarization variation based on 180° polarization switching. The model is applicable to the materials showing 180° or nearly 180° polarization switching such as SrBi₂Nb₂O₉, Bi₄Ti₃O₁₂, Bi_{4-x}Ln_xTi₃O₁₂ (Ln = La, Nd, Sm), LiTaO₃, and LiNaO₃, [66-72].

APPENDIX: SUMMARY OF EXPERIMENTAL RESULTS OF FeFETs

EKAI model was developed and verified using experimental data of FeFETs consisting of MFIS gate stacks of Ir/CSBT/HfO₂/IL/Si. Manufacturing details of the FeFETs were explained elsewhere [73]. The thicknesses of CSBT and HfO₂ were 135 nm and 4 nm, respectively. The interfacial layer (IL) was formed on the silicon substrate surface during the crystallization annealing by which the ferroelectricity appeared in the CSBT. The IL was an amorphous SiO₂ with the thickness of 2.6 nm according to the cross-sectional observation by transmission electron microscopy. The insulator (I) layer of the MFIS was composed of double layers of the HfO₂ and the IL. Since the dielectric constants of SiO₂ and HfO₂ are 3.9 and about 20, respectively, the I layer is characterized by $d_i = 3.5$ nm, $\varepsilon_i = 3.9$, and $C_i = 0.99$ $\mu\text{F}/\text{cm}^2$ in the calculation scheme. Gate metal length L_m was 10 μm . Channel length L was 8 μm as a distance between the source and drain edges, implying that the overlap lengths were 1 μm for both gate-and-drain and gate-and-source. The FeFETs of various gate widths (W) from 10 μm to 200 μm were on a chip ready for experimental data measurements.

To get the thin IL, the FeFETs were annealed for the CSBT crystallization in an N₂ main gas mixed with a small amount of O₂. We found the mixing ratio of the ambient gas changed the CSBT crystal orientations in FeFETs during the annealing. EBSD showed that orientation amount *vs.* the angle θ was distributed almost flat in O₂ annealed FeFETs [21] but not flat in N₂ dominant annealed FeFETs [74]. The FeFETs adopted in the present work are the ones annealed in the ambient N₂ dominant, where the orientation is unevenly distributed; major grains have $\theta \geq 65^\circ$ [74] as shown in Fig. 7.

Three kinds of experimental data are compared to numerical results by the EKAI model calculations, *i.e.*,

- (1) drain current (I_d) *versus* gate voltage (V_g),
- (2) Induced charge Q_m in the metal gate *versus* V_g , and
- (3) V_g -pulse write and V_{th} read, *i.e.*, PWVR.

(1) Experimental I_d - V_g

I_d - V_g curves were obtained using a semiconductor parameter analyzer (Agilent 4156C), in which the V_g sweeping was quasi-statically slow. The experimental curves of an n -channel FeFET are shown in Fig. A1. The source voltage V_s and the substrate voltage V_{sub} were 0 V, and the drain voltage $V_d = 0.1$ V. The I_d was normalized by W/L , and V_{th} was defined as the V_g at $I_d = 10^{-8}$ A.

The memory window V_w is defined by $V_{thr} - V_{thl}$, where the threshold voltage V_{thr} (V_{thl}) is on the right- (left-) side on the $I_d - V_g$ hysteresis curve. With increasing the V_g sweep amplitude, V_w was increased (the inset of Fig. A1) due to increased polarization switching. By using Ir [75] or Pt [3] as a gate metal, SBT or CSBT FeFETs could have long retention and high endurance [3,75]. Since the work functions of Pt and Ir [76] are larger than the fermi level of p -type Si substrates, the SBT or CSBT FeFETs originally have a larger V_{thl} than 1 V [3,77]. Practically, FeFETs with nearly 0 V for $(V_{thr} + V_{thl})/2$ are preferred, thus carrier concentrations are controlled by n -type shallow doping in the Si channel [73,78]. By adjusting the dose and energy of the dopants, V_{thl} and V_{thr} can be shifted to negative by more than 1 V at the cost of increase in off-state I_d . In the $I_d - V_g$ curves as shown in Fig. A1, a high off-state current of 10^{-12} A order is due to the channel surface doping. In the calculation scheme of this paper, this surface doping effect is treated as an adjustment of the flat-band voltage V_{fb} with negative values. Presence of a large surface state density, D_{it} , in the channel is suggested by large SS (subthreshold swing) values of 140 mV/decade at around $I_d = 10^{-9}$ A. As shown in Fig. A1, I_d increases with decreasing V_g below about - 1 V. This is the gate-induced drain leakage (GIDL) current [79, 3]. Due to the overlapped large area of the gate and drain, a p -type inversion layer is formed at the surface of the drain beneath the gate metal, when a negative V_g is applied. This p -inversion forms a reverse-biased $p - n$ junction in the n -drain region. Since the impurity concentration is heavy in the drain, the reverse-biased junction easily accompanies a tunnel current. The GIDL is closed in the substrate and related neither to the gate ferroelectric defects nor the gate leakage current between the gate and silicon. If one chooses a structure with negligible gate-and-drain overlapping, the GIDL current can be diminished. When we used a self-aligned gate structure, this current was indeed decreased [80].

(2) Experimental $Q_m - V_g$

Q_m vs. V_g curves were obtained using a ferroelectric test system (RT6000S, Radiant Technology). The gate is connected to one terminal of the system, and the substrate, source, and drain are connected to the other terminal. The measurement time between the neighboring two points is 1.16 ms, meaning that if 200 measurement points are assigned for one loop, it takes 0.23 s to measure one loop. The experimentally obtained Q_m vs. V_g curves with several V_g sweep amplitudes are shown in Fig. A2. Because of the MFIS structure if we fix Q_m and assume no charge injection, V_g is the summation of the voltages across the ferroelectric and across the insulator, and the surface potential of the silicon channel. The curves in the first quadrant of the $Q_m - V_g$ coordinates include the depletion state of the semiconductor surface side, and those in the third quadrant do not include it. Hence, the curves are asymmetric for the origin of the coordinate. Despite the semiconductor surface depletion, the curve variation with changing V_g in Fig. A2 is smoother than expected. This smoother phenomenon can also be explained by charge occupation and release in a rather high interface state density presented at the silicon channel surface. The gradient of the curves in the third quadrant can be utilized to decide the permittivity

of the linear paraelectric component, ε_{fdi} , of the ferroelectric because the depletion state is not included in this side.

(3) Experimental PWVR

Two threshold voltages V_{thn} and V_{thp} were defined in PWVR. The V_{thn} was measured after a negative single pulse V_g with height (V_l) and width (t_w). The V_{thp} was measured after a positive single pulse V_g with height ($V_h = -V_l$) and t_w . The difference ΔV_{th} was evaluated by $\Delta V_{th} = V_{thn} - V_{thp}$ as a function of V_h and V_l at various t_w . The PWVR measurement was performed according to the schematic chart (Fig. A3). In FeFETs, no full saturation of ferroelectric polarization is allowed. If we would make the ferroelectric polarization fully saturated, we must apply large V_g which leads to charge injection and traps unacceptable for FeFETs. As the consequence of the unsaturated polarizations, any threshold voltage V_{th} of the FeFETs are not defined using a specific reference value. In other words, a single V_{th} has no meaning to identify the memory state of a FeFET which can only be recognized relatively by a difference ΔV_{th} from the previous V_{th} . Hence, we use a pair of write voltages, (V_h, t_w) and (V_l, t_w) with $V_l = -V_h$. Idling cycles of the pairs of pulses were given plural times before performing the write and read operation. The role of the idling cycles is to obtain V_{th} unaffected by the history of the previous operations. In our experiment, as shown in Fig. A3, after the twice idling a write (V_l, t_w) pulse is applied then V_{thp} is read by sweeping V_g in a narrow range from V_{swp_start} to V_{swp_end} . Next, a write (V_h, t_w) pulse is applied then V_{thn} is read by sweeping V_g in the same range as the V_{thp} read. During the idling and the writing, $V_d = V_s = V_{sub} = 0$ V. During the read, $V_d = 0.1$ V and $V_s = V_{sub} = 0$ V. Time length of the read by sweeping V_g was of the order of 1 s. V_g was applied by a pulse generator Agilent 81110A, and I_d was measured by Agilent 4156C. Our homemade program codes written by the LabVIEW controlled these machines. Figure A4 shows the experimental results of PWVR. The figure shows that ΔV_{th} varies linearly with $\log(t_w)$. These log-linear properties have been commonly obtained for SBT- FeFETs [81] and CSBT- FeFETs [5,6] reported previously. In writing, t_w was changed from 100 ns to 1 ms, with $V_h = 3$ V, 4 V, 5 V, 6V. In reading, $V_{swp_start} = 0$ V, $V_{swp_end} = 1.4$ V, and $V_d = 0.1$ V. Write pulses with combinations of long t_w and high $V_h = -V_l = 5$ V and 6 V were not applied to avoid charge injection and trap in the FeFET.

-
1. Y. Tarui, T. Hirai, K. Teramoto, H. Koike, and K. Nagashima, *Application of the ferroelectric materials to ULSI memories*, Appl. Surf. Sci. **113-114** 656 (1997). Doi.10.1016/S0169-4332(96)00963-4
 2. B.-E. Park, H. Ishiwarra, M. Okuyama, S. Sakai, S.-M. Yoon, Editors, *Ferroelectric-gate field effect transistor memories – Device Physics and Applications* 2nd ed. (Springer, Nature, Singapore, 2020).
 3. S. Sakai and R. Ilangovan, *Metal-ferroelectric-insulator-semiconductor memory FET with long retention and high endurance*, IEEE Electron Device Lett. **25** 369 (2004). Doi: 10.1109/LED.2004.828992
 4. W. Zhang, M. Takahashi and S. Sakai, *Electrical properties of $\text{Ca}_x\text{Sr}_{1-x}\text{Bi}_2\text{Ta}_2\text{O}_9$ ferroelectric-gate field-*

- effect transistors*, Semicond. Sci. Technol. 28 085003 (2013). Doi:10.1088/0268-1242/28/8/085003
5. L. V. Hai, M. Takahashi, W. Zhang, and S. Sakai, *100-nm-size ferroelectric-gate field-effect transistor with 10⁸-cycle endurance*, Jpn J. Appl. Phys. **54**, 088004 (2015). Doi: 10.7567/JJAP.54.088004
 6. M. Takahashi and S. Sakai, *Area-scalable 10⁹-cycle-high-endurance FeFET of strontium bismuth tantalate using a dummy-gate process*. Nanomaterials **2021**, 11, 101. Doi: 10.3390/nano11010101
 7. A. F. Devonshire, *Theory of barium titanate*, Phil. Mag. J. Sci., **40:309**, 1040 (1949). Doi: 10.1080/14786444908561372
 8. M. E. Lines, A. M. Glass, *Principles and Applications of Ferroelectrics and Related Materials* (Oxford University Press, New York, 1977).
 9. R. Tilley and B. Zeks, *Landau theory of phase transitions in thick films*, Solid State Commun. 49 823 (1984). Doi: 10.1016/0038-1098(84)90089-9
 10. V. A. Zhirnov, *A contribution to the theory of domain walls in ferroelectrics*, Sov. Phys. JETP, **35** 822 (1959).
 11. E. V. Chenskii, *Thermodynamic relations for the domain structure of ferroelectrics*, Sov Phys Solid State **14**, 1940 (1973).
 12. Y. L. Li, S. Y. Hu, Z. K. Liu, and L. Q. Chen, *Effect of substrate constraint on the stability and evolution of ferroelectric domain structures in thin films*, Acta Materialia **50**, 395 (2002). Doi: 10.1016/S1359-6454(01)00360-3
 13. K. Dayal and K. Bhattacharya, *A real-space non-local phase-field model of ferroelectric domain patterns in complex geometries*, Acta Materialia **55** 1907 (2007). Doi: 10.1016/j.actamat.2006.10.049
 14. C. E. Krill and L.-Q. Chen, *Computer simulation of 3-D grain growth using a phase field model*, Acta Materialia **50**, 3057 (2002). Doi: 10.1016/S1359-6454(02)00084-8
 15. L. D. Landau and I. M. Khalatnikov, *On the anomalous absorption of sound near a second order transition point* [in Russian], Doklady Akademii Nauk, SSSR, 96 469 (1954). English translation in collected papers of Landau, edited by D. Ter Haar, 626 (1951).
 16. V. C. Lo and Z. J. Chen, *Simulation of the effects of space charge and Schottky barriers on ferroelectric thin film capacitor using Landau Khalatnikov theory*, IEEE Trans. Ultrason. Ferroelectr. Freq. Control **49**, 980 (2002). Doi: 10.1109/TUFFC.2002.1020168
 17. G. Vitzrik, S. Ducharme, V. M. Fridkin, and S. G. Yudin, *Kinetics of ferroelectric switching in ultrathin films*, Phys. Rev B **68**, 094113 (2003), Doi: 10.1103/PhysRevB.68.094113
 18. H.-L. Hu and L.-Q. Chen, *Three-dimensional computer simulation of ferroelectric domain formation*, J. Am. Ceram. Soc., **81** 492 (1998). Doi: 10.1111/j.1151-2916.1998.tb02367.x
 19. L. D. Landau and E. M. Lifshitz, *Statistical Physics*, 2nd Revised and Enlarged Edition (Pergamon Press, 1969), p. 380 in Chap. XII.
 20. A. R. Geivandov, S. P. Palto, S. G. Yudin, and L. M. Blinov, *Switching time dispersion and retention of bistable states in Langmuir-Blodgett ferroelectric films*, J. Exp. and Theor. Phys., **99**, 83 (2004). Doi: 10.1134/1.1787081
 21. W. Zhang, M. Takahashi, and S. Sakai, *Investigation of ferroelectric grain sizes and orientations in Pt/Ca_xSr_{1-x}Bi₂Ta₂O₉/Hf-Al-O/Si high performance ferroelectric-gate field-effect-transistors*, Materials **12**,

399 (2019). DOI:10.3390/ma12030399

22. G. D. Hu, J. B. Xu, and I. H. Wilson, *Domain imaging and local piezoelectric properties of the (200)-predominant SrBi₂Ta₂O₉ thin film*, Appl. Phys. Lett. **75**, 1610 (1999). Doi: 10.1063/1.124770
23. A. Gruverman, A. Pignolet, K. M. Satyalakshmi, M. Alexe, N. D. Zakharov, and D. Hesse, *Nanosopic switching behavior of epitaxial SrBi₂Ta₂O₉ films deposited by pulsed laser deposition*, Appl. Phys. Lett. **76**, 106 (2000). Doi: 10.1063/1.125671
24. J. S. Liu, S. R. Zhang, H. Z. Zeng, W. D. Fei, and S. Y. Du, *90° switching of polarization in La³⁺-doped SrBi₂Ta₂O₉ thin films*, J. Appl. Phys. **99**, 094103 (2006). Doi: 10.1063/1.2195015
25. L. Z. Li, P. Gao, C. T. Nelson, J. R. Jokisaari, Yi Zhang, S.-J. Kim, A. Melville, C. Adamo, D. G. Schlom, and X. Q. Pan, *Atomic scale structure changes induced by charged domain walls in ferroelectric materials*, Nano Lett., **13**, 5218–5223 (2013). Doi:10.1021/nl402651r
26. L. Z. Li, J. Britson, J. R. Jokisaari, Y. Zhang, C. Adamo, A. Melville, D. G. Schlom, L.-Q. Chen, and X. Q. Pan, *Giant resistive switching via control of ferroelectric charged domain walls*, Adv. Mater., **28**, 6574 (2016). Doi: 10.1002/adma.201600160
27. A. N. Kolmogorov, *On the Statistical Theory of Crystallization of Metals* [in Russian], Izv. Akad. Nauk SSSR, Ser. Mat., **3**, 355 (1937). See also G.S. Zhdanov, *Crystal Physics*, translated and edited by A. F. Brown (Oliver & Boyd, Edinburgh 1965) p. 378.
28. M. Avrami, *Kinetics of Phase Change. I General Theory*, J. Chem. Phys. **7**, 1103 (1939). Doi: 10.1063/1.1750380 M. Avrami, *Kinetics of Phase Change. II Transformation-Time Relations for Random Distribution of Nuclei*, J. Chem. Phys. **8**, 212 (1940). Doi: 10.1063/1.1750631 M. Avrami, *Granulation, Phase Change, and Microstructure Kinetics of Phase Change. III*, J. Chem. Phys. **9**, 177 (1941). Doi: 10.1063/1.1750872
29. Y. Ishibashi and Y. Takagi, *Note on ferroelectric domain switching*, J. Phys. Soc. Japan. **31**, 506 (1971). Doi: 10.1143/JPSJ.31.506
30. Y. W. So, D. J. Kim, and T. W. Noh, *Polarization switching kinetics of epitaxial Pb(Zr_{0.4}Ti_{0.6})O₃*, Appl. Phys. Lett. **86**, 092905 (2005). Doi: 10.1063/1.1870126
31. W. Li and M. Alexe, *Investigation on switching kinetics in epitaxial Pb(Zr_{0.2}Ti_{0.8})O₃ ferroelectric thin films: Role of the 90° domain walls*, Appl. Phys. Lett. **91**, 262903 (2007). Doi:10.1063/1.2825414
32. O. Lohse, M. Grossmann, U. Boettger, D. Bolten, and R. Waser, *Relaxation mechanism of ferroelectric switching in Pb(Zr,Ti)O₃ thin films*, J. Appl. Phys. **89**, 2332 (2001). Doi:10.1063/1.1331341
33. A. K. Tagantsev, I. Stolichnov, N. Setter, J. S. Cross, and M. Tsukada, *Non-Kolmogorov-Avrami switching kinetics in ferroelectric thin films*, Phys. Rev B **66** 214109 (2002). Doi: 10.1103/PhysRevB.66.214109
34. H. Mulaosmanovic, J. Ocker, S. Müller, U. Schroeder, J. Müller, P. Polakowski, S. Flachowsky, R. van Bentum, T. Mikolajick, and S. Slesazeck, *switching kinetics in nanoscale hafnium oxide based ferroelectric field-effect transistors*, ACS Appl. Mater. Interfaces **9**, 3792 (2017). Doi:10.1021/acsami.6b13866
35. T. S. Böske, J. Müller, D. Bräuhäus, U. Schröder and U. Böttger, *Ferroelectricity in hafnium oxide: CMOS compatible ferroelectric field effect transistors, 2011 International Electron Devices Meeting*, (Washington, DC, USA, 2011) pp. 24.5.1-24.5.4. Doi: 10.1109/IEDM.2011.6131606.

36. N. Gong and T. -P. Ma, *A study of endurance issues in HfO₂-based ferroelectric field effect transistors: Charge trapping and trap generation*, IEEE Electron Device Lett., **39**, 15 (2018). Doi: 10.1109/LED.2017.2776263
37. K. Toprasertpong, M. Takenaka and S. Takagi, *Direct observation of interface charge behaviors in FeFET by quasi-static split C-V and Hall techniques: Revealing FeFET operation*, 2019 IEEE International Electron Devices Meeting, (San Francisco, CA, USA, 2019) pp. 23.7.1-23.7.4. Doi: 10.1109/IEDM19573.2019.8993664.
38. J. Tan *et al.*, *Ferroelectric HfO₂ memory transistors with high- κ interfacial layer and write endurance exceeding 10¹⁰ cycles*, IEEE Electron Device Lett., **42**, 994 (2021). Doi: 10.1109/LED.2021.3083219.
39. T. Mikolajick, S. Slesazeck, H. Mulaosmanovic, M. H. Park, S. Fichtner, P. D. Lomenzo, M. Hoffmann, and U. Schroeder, *Next generation ferroelectric materials for semiconductor process integration and their applications*, J. Appl. Phys. **129**, 100901 (2021). Doi: 10.1063/5.0037617
40. Y. Ishibashi, *Polarization reversal in ferroelectrics* [in Japanese], Ouyoubutsuri **67**, 1249 (1998). Doi: 10.11470/oubutsu1932.67.1249
41. W. J. Merz, *Domin formation and domain wall motions in ferroelectric BaTiO₃ single crystals*, Phys. Rev, **95**, 690 (1954). Doi: 10.1103/PhysRev.95.690
42. E. Fatuzzo and W. J. Merz, *Switching Mechanism in Triglycine sulfate and other ferroelectrics*, Phys. Rev. **116** 61 (1959). Doi: 10.1103/PhysRev.116.61
43. T. Tybell, P. Paruch, T. Giamarchi, and J.-M. Triscone, *Domain wall creep in epitaxial ferroelectric Pb(Zr_{0.2}Ti_{0.8})O₃ thin films*, Phys. Rev. Lett. **89**, 097601 (2002). Doi: 10.1103/PhysRevLett.89.097601
44. P. Paruch, T. Giamarchi, T. Tybell, and J.-M. Triscone, *Nanoscale studies of domain wall motion in epitaxial ferroelectric thin films*, J. Appl. Phys. **100**, 051608 (2006). Doi: 10.1063/1.2337356
45. D. J. Kim, J. Y. Jo, T. H. Kim, S. M. Yang, B. Chen, Y. S. Kim, and T. W. Noh, *Observation of inhomogeneous domain nucleation in epitaxial Pb(Zr,Ti)O₃ capacitors*, Appl. Phys. Lett. **91**, 132903 (2007). Doi: 10.1063/1.2790485
46. J. Y. Jo, S. M. Yang, T. H. Kim, H. N. Lee, J.-G. Yoon, S. Park, Y. Jo, M. H. Jung, and T. W. Noh, *Nonlinear dynamics of domain-wall propagation in epitaxial ferroelectric thin films*, Phys. Rev. Lett. **102**, 045701 (2009). Doi: 10.1103/PhysRevLett.102.045701
47. S. Liu, I. Grinberg, and A. M. Rappe, *Intrinsic ferroelectric switching from first principles*, Nature **534**, 360 (2016). Doi:10.1038/nature18286
48. S. Sakai, X. Zhang, L. Van Hai, W. Zhang, and M. Takahashi, *Downsizing and memory array integration of Pt/SrBi₂Ta₂O₉/Hf-Al-O/Si ferroelectric-gate field-effect transistors*, 2012 12th Annual Non-Volatile Memory Technology Symposium (Singapore, 2012) pp. 55-59. Doi: 10.1109/NVMTS.2013.6632862.
49. S. Sakai, W. Zhang, and M. Takahashi, *Method for disclosing invisible physical properties in metal–ferroelectric–insulator–semiconductor gate stacks*, J. Phys. D: Appl. Phys. **50**, 165107 (2017). Doi: 10.1088/1361-6463/aa622f
50. S. M. Sze, *Physics of Semiconductor Devices 2nd ed.* (John Wiley & Sons, New York, 1981) in Chapters 7–8.

51. C. P. de Araujo, J. D. Cuchiaro, L. D. McMillan, M. C. Scott, and J. F. Scott, *Fatigue-free ferroelectric capacitors with platinum electrodes*, Nature **374**, 627 (1995). Doi.org/10.1038/374627a0
52. Y. Shimakawa, Y. Kubo, and F. Izumi, *Crystal structure and ferroelectric properties of $ABi_2Ta_2O_9$ ($A=Ca, Sr$, and Ba)*, Phys. Rev. B **61**, 6559 (2000). Doi: 10.1103/PhysRevB.61.6559
53. P. Paruch and J. Guyonnet, *Nanoscale studies of ferroelectric domain walls pinned elastic interfaces*, C. R. Physique **14** 667 (2013). Doi: 10.1016/j.crhy.2013.08.004
54. N. A. Pertsev, A. Petraru, H. Kohlstedt, R. Waser, I. K. Bdikin, D. Kiselev, and A. L. Kholkin, *Dynamics of ferroelectric nanodomains in $BaTiO_3$ epitaxial thin films via piezoresponse force microscopy*, Nanotechnology **19**, 375703 (2008). DOI: 10.1088/0957-4484/19/37/375703
55. P. Paruch, T. Giamarchi, and J.-M. Triscone, *Domain wall roughness in epitaxial ferroelectric $PbZr_{0.2}Ti_{0.8}O_3$ thin films*, Phys. Rev. Lett. **94**, 197601 (2005). Doi: 10.1103/PhysRevLett.94.197601
56. Z. Xiao, S. Poddar, S. Ducharme, and X. Hong, *Domain wall roughness and creep in nanoscale crystalline ferroelectric polymers*, Appl. Phys. Lett. **103**, 112903 (2013). Doi: 10.1063/1.4820784
57. R. C. Miller and G. Weinreich, *Mechanism for the sidewise motion of 180° domain walls in barium titanate*, Phys. Rev. **117**, 1460 (1960). Doi: 10.1103/PhysRev.117.1460
58. Y.-H. Shin, I. Grinburg, I.-W. Chen, and A. M. Rappe, *Nucleation and growth mechanism of ferroelectric domain-wall motion*, Nature **449**, 882 (2007). Doi:10.1039/nature06165
59. D. Zhao, I. Katsouras, K. Asadi, P. W. M. Blom, and D. M. de Leeuw, *Switching dynamics in ferroelectric $P(VDF-TrFE)$ thin films*, Phys. Rev B **92**, 214115 (2015). Doi: 10.1103/PhysRevB.92.214115
60. Y. Ishibashi, *Computational method of activation energy of thick domain walls*, J. Phys. Soc. Japan **46**, 1254 (1979). Doi: 10.1143/JPSJ.46.1254
61. P. Marton, I. Rychetsky, and J. Hlinka, *Domain walls of ferroelectric $BaTiO_3$ within the Ginzburg-Landau-Devonshire phenomenological model*, Phys. Rev. B **81**, 144125 (2010). Doi: 10.1103/PhysRevB.81.144125
62. M. Fukuda, W. Mizubayashi, A. Kohno, S. Miyazaki, and M. Hirose, *Analysis of tunnel current through ultrathin gate oxides*, Jpn. J. Appl. Phys. **37**, L1534 (1998). Doi: 10.1143/JJAP.37.L1534
63. L. F. Register, E. Posenbaum, and K. Yang, *Analytic model for direct tunneling current in polycrystalline silicon-gate metal-oxide-semiconductor devices*, Appl. Phys. Lett. **74**, 457 (1999). Doi: 10.1063/1.123060
64. S. Salahuddin and S. Datta, *Can the subthreshold swing in a classical FET be lowered below 60 mV/decade? 2008 IEEE International Electron Devices Meeting*, (San Francisco, CA, USA, 2008) pp, 1-4. Doi: 10.1109/IEDM.2008.4796789
65. T. Watanabe, T. Sakai, H. Funakubo, K. Saito, M. Osada, M. Yoshimoto., A. Sasaki., J. Liu, and M. Kakihana, *Ferroelectric property of a -/ b -axis-oriented epitaxial $Sr_{0.8}Bi_{2.2}Ta_2O_9$ thin films grown by metalorganic chemical vapor deposition*, Jpn. J. Appl. Phys. **41**, L1478 (2002). Doi: 10.1143/JJAP.41.L1478
66. J. Lettieri, M. A. Zurbuchen, Y. Jia, D. G. Schlom, S. K. Streiffer, and M. E. Hawley, *Epitaxial growth of $SrBi_2Nb_2O_9$ on (110) $SrTiO_3$ and the establishment of a lower bound on the spontaneous polarization of $SrBi_2Nb_2O_9$* , Appl. Phys. Lett. **77** 3090 (2000). Doi: 10.1063/1.1322055

67. M. Azodi, C. Harnagea, V. Buscaglia, M. T. Buscaglia, P. Nanni, F. Rosei, and A. Pignolet, *Ferroelectric switching in $\text{Bi}_4\text{Ti}_3\text{O}_{12}$ nanorods*, IEEE Trans. Ultrason. Ferroelectr. Freq. Control **59** 1903 (2012). Doi: 10.1109/TUFFC.2012.2405
68. B. H. Park, B. S. Kang, S. D. Bu, T. W. Noh, and W. Jo, *Lanthanum-substituted bismuth titanate for use in non-volatile memories*, Nature **401**, 682 (1999). Doi.org/10.1038/44352
69. T. Sakai, T. Watanabe, H. Funakubo, K. Saito, and M. Osada, *Effect of La substitution on electrical properties of highly oriented $\text{Bi}_4\text{Ti}_3\text{O}_{12}$ films prepared by metalorganic chemical vapor deposition*, Jpn. J. Appl. Phys. **42**, 166 (2003). Doi: 10.1143/JJAP.42.166
70. A. Garg, A. Snedden, P. Lightfoot, J. F. Scott, X. Hu and Z. H. Barber, *Investigation of structural and ferroelectric properties of pulsed-laser-ablated epitaxial Nd-doped bismuth titanate films*, J. Appl. Phys. **96**, 3408 (2004). Doi: 10.1063/1.1766097
71. Z. X. Cheng, C. V. Kannan, K. Ozawa, H. Kimura, X. L. Wang, *Orientation dependent ferroelectric properties in samarium doped bismuth titanate thin films grown by the pulsed-laser-ablation method*, Appl. Phys. Lett. **89**, 032901 (2006). Doi: 10.1063/1.2221918
72. V. Y. Shur, *Kinetics of ferroelectric domains: Application of general approach to LiNbO_3 and LiTaO_3* , J. Mater. Sci **41** **199** (2006). Doi: 10.1007/s10853-005-6065-7
73. W. Zhang, M. Takahashi, Y. Sasaki, M. Kusuhara, and S. Sakai, *3.3V write-voltage $\text{Ir}/\text{Ca}_{0.2}\text{Sr}_{0.8}\text{Bi}_2\text{Ta}_2\text{O}_9/\text{HfO}_2/\text{Si}$ ferroelectric-gate field-effect transistors with 10^9 endurance and good retention*, Jpn. J. Appl. Phys. **56**, 04CE04 (2017). Doi: 10.7567/JJAP.56.04CE04
74. W. Zhang, M. Takahashi, and S. Sakai, unpublished.
75. S. Sakai, W. Zhang, and M. Takahashi, *Dynamic analog characteristics of 10^9 Cycle-endurance low-voltage nonvolatile ferroelectric-gate memory transistors*, 2017 IEEE International Memory Workshop (Monterey, CA, USA, 2017) pp. 1-4. Doi: 10.1109/IMW.2017.7939080
76. S. M. Sze, *Physics of Semiconductor Devices 2nd ed.* (John Wiley & Sons, New York, 1981), in Chapter 5.
77. S. Sakai, R. Ilangovan, and M. Tahahashi, *$\text{Pt}/\text{SrBi}_2\text{Ta}_2\text{O}_9/\text{Hf-Al-O}/\text{Si}$ field-effect-transistor with long retention using unsaturated ferroelectric polarization switching*, Jpn J. Appl. Phys. **43**, 7876 (2004). Doi: 10.1143/JJAP.43.7876
78. M. Takahashi, W. Zhang and S. Sakai, *High-endurance ferroelectric NOR flash memory using $(\text{Ca},\text{Sr})\text{Bi}_2\text{Ta}_2\text{O}_9$ FeFETs*, 2018 IEEE International Memory Workshop (Kyoto, Japan, 2018) pp. 1-4. Doi: 10.1109/IMW.2018.8388835
79. J. Chen, T. Y. Chan, I. C. Chen, P. K. Ko, and C. Hu, *Sub-breakdown drain leakage current in MOSFET*, IEEE Electron Device Lett. **8**, 515 (1987). Doi: 10.1109/EDL.1987.26713
80. M. Takahashi and S. Sakai, *Self-aligned-gate metal/ferroelectric/insulator/semiconductor field-effect transistors with long memory retention*, Jpn J. Appl. Phys. **44**, L800 (2005). Doi: 10.1143/JJAP.44.L800
81. S. Wang, M. Takahashi, Q. H. Li, K. Takeuchi, and S. Sakai, *Operational method of a ferroelectric (Fe)-NAND flash memory array*, Semicond. Sci. Technol. **24**, 105029 (2009). Doi: 10.1088/0268-1242/24/10/105029de

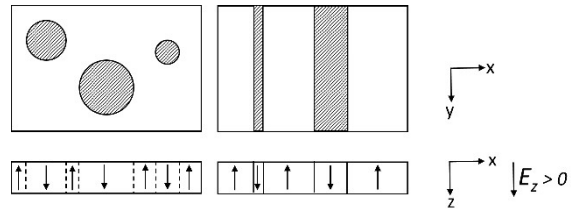


FIG. 1 KAI schematic drawing of domain nucleation and growth in a film under an electric field parallel to the z -axis ($E_z > 0$). The uppers and lowers are top- and side-views, respectively. The lefts and rights represent two- and one-dimensional nucleation and growth manners, respectively. The shaded areas are on the way to expansion. An analytical function of the KAI model (Eq.(2)) describes the volume fraction increase of the downward (upward) domain with time under a constant positive (negative) E_z .

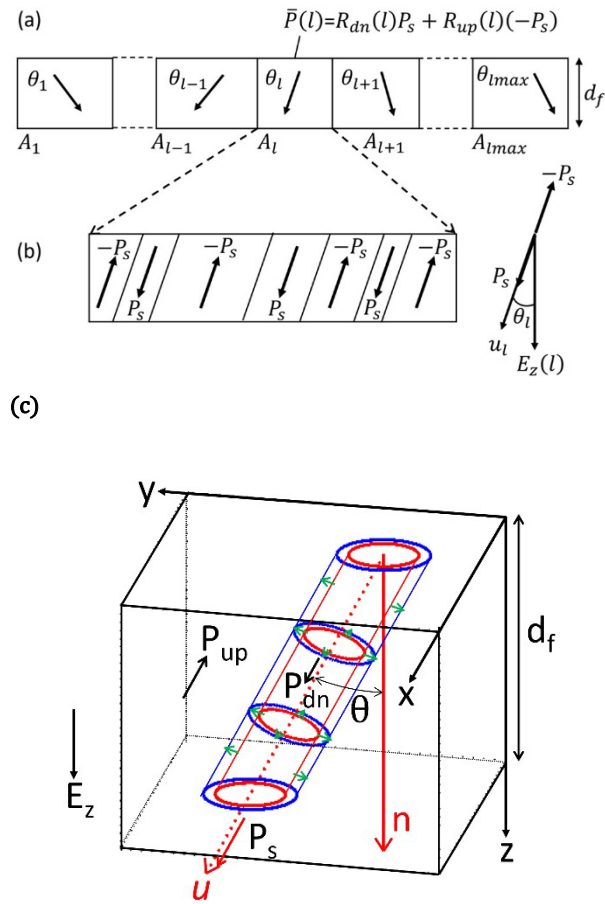


FIG. 2 (a) EKA schematic picture of a ferroelectric film constituted by polycrystalline grains. Grain l has an orientation angle θ_l and area A_l . θ_l is the angle between the z -axis and the u_l axis. The u_l axis is parallel to the spontaneous polarization P_s . (b) Grain l consists of downward (P_s) and upward ($-P_s$) domain regions. The P_s direction in the upward (downward) domains is parallel (anti-parallel) to the u_l axis. (c) A scheme of the EKA model. A polarization nucleus is formed along the u -direction and the domain wall spreads laterally to the u -direction.

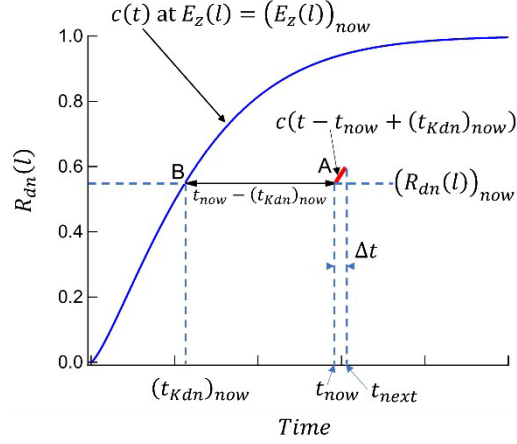


FIG. 3 Concept of the EKAI model when the electric field changes with time. In the case of E_z varying with time, let us consider a case in grain l that, at $t = t_{now}$, $R_{dn}(l)$ is $(R_{dn}(l))_{now}$ under $E_z(l) = (E_z(l))_{now}$. This status is the point A in the graph. Draw a curve of the EKAI function (Eq. (11)) at a constant field, $E_z(l) = (E_z)_{now}$, as the blue solid line $c(t)$ ((Eqs.(2) and (11))). The point on the curve $c(t)$ at $R_{dn}(l) = (R_{dn}(l))_{now}$ is B, and the time at the point B is $(t_{Kdn})_{now}$. We assume that the growth of $(R_{dn}(l))_{now}$ from $t = t_{now}$ to $t = t_{now} + \Delta t = t_{next}$ with $E_z(l) = (E_z(l))_{now}$ at point A is the same as the growth of $(R_{dn}(l))_{now}$ at point B under the same constant field $(E_z(l))_{now}$. The $R_{dn}(l)$ growth during Δt at the point A can thus be calculated by a parallel-shifted function, $c(t - t_{now} + (t_{Kdn})_{now})$, and $(R_{dn}(l))_{next}$ is obtained as Eq. (19). At $t = t_{next} + \Delta t$ the same procedure is repeated under a varied new- $E_z(l)$, and we obtain $R_{dn}(l)$ at $t = t_{next} + \Delta t$. The same is performed for $R_{up}(l)$ in the case of $E_z(l) < 0$, and $(R_{up}(l))_{next}$ is derived as Eq. (22).

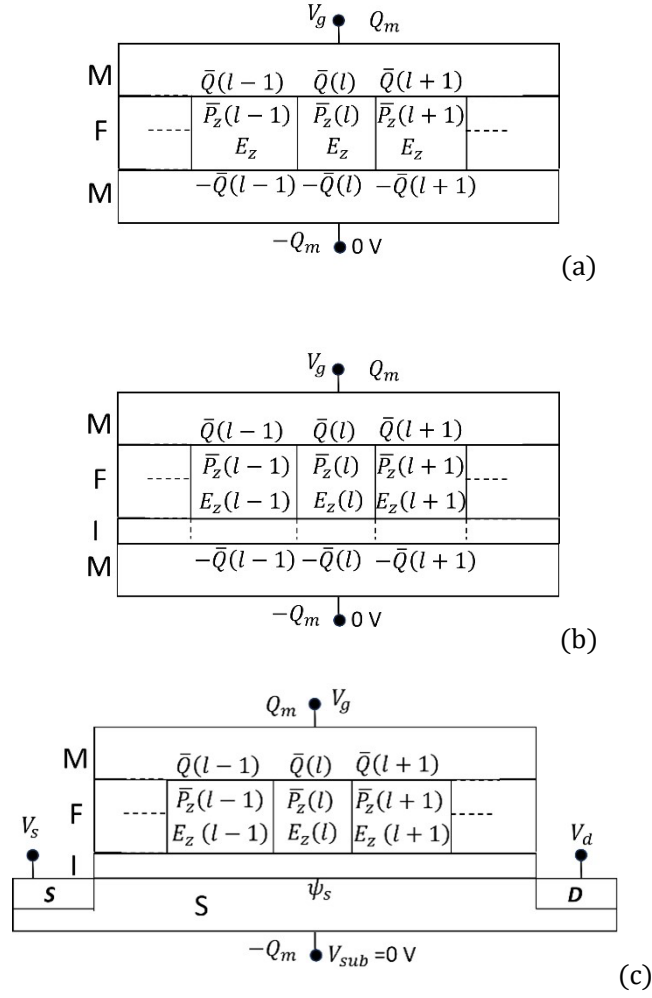


FIG. 4 Total calculation scheme for specific devices. (a) an MFM capacitor. (b) an MFIM capacitor. (c) an MFIS FeFET. The EKAI model under a varying field E_z with time provides $\bar{P}_z(l)$, $R_{dn}(l)$, and $R_{up}(l)$ at $t = t_{next}$ using $R_{dn}(l)$, $R_{up}(l)$, and $E_z(l)$ at $t = t_{now}$. To repeat calculation, it is necessary to obtain $E_z(l)$ at $t = t_{next}$. Depending on the structure of the specific devices, the method of deriving $E_z(l)$ is different. For an MFM capacitor case (a), $E_z(l)$ does not depend on l , and E_z at $t = t_{next}$ is obtained by Eq. (33). For an MFIM capacitor case (b), the induced charges of the bottom electrode of grain l , $-\bar{Q}(l)$ is a good approximation. $E_z(l)$ depends on l . $Q(l)$ at $t = t_{next}$ is derived by Eq. (38). Then $E_z(l)$ at $t = t_{next}$ is obtained by Eq. (37). For an MFIS FeFET case (c), D_z at the top surface of the insulator is averaged over all the grains due to a transitional thin layer between the ferroelectric and the insulator. (See Fig. 5.) The surface potential ψ_s of the semiconductor is assumed to be uniform because of insufficient acceptor density N_A . The uniform D_z and ψ_s lead to a grain-independent field E_z [$E_z(l) = E_z$ for all l]. ψ_s at $t = t_{next}$ is derived by Eq. (42). Then, Q_m is obtained from Eq. (44), and E_z is obtained from Eq. (40).

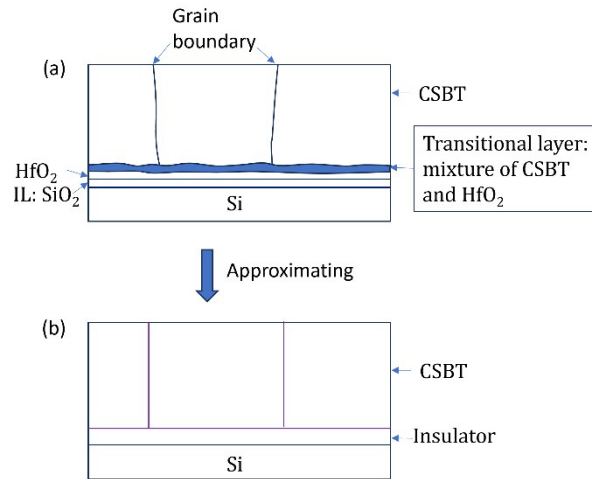


FIG. 5 (a) Schematic cross section of the experimental MFIS FeFETs. (b) The approximate structure assumed in the EKAI. In the experimental, the insulator is the bilayer of a 4 nm-thick HfO₂ layer and a 2.6 nm-thick IL (SiO₂) layer. The ferroelectric CSBT is 135 nm thick. A transitional layer exists at the interface between the CSBT and HfO₂ layers. A photo of a cross-section TEM confirmed this layer presence [73]. The transitional layer (≈ 5 nm thick) is constituted by fine grains. The TEM photo contrast indicates that main atom elements are of the CSBT. Since a CSBT-originated high permittivity can be assumed, $D_z(l)$ is expected to be averaged of this transitional layer. Therefore, we can approximate the structure as (b) in this figure. D_z is averaged over all the grains at the top surface of the insulator.

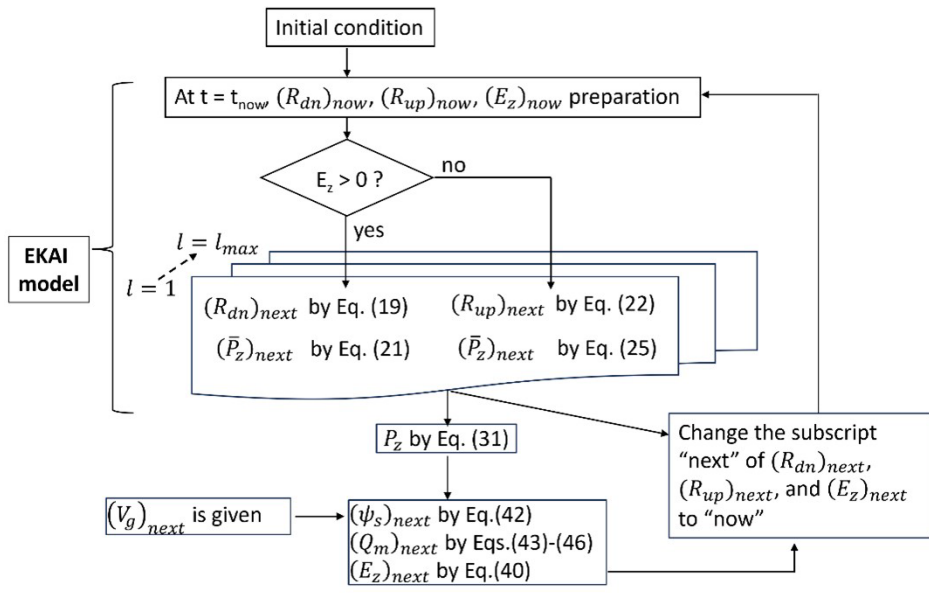


FIG. 6 Calculation scheme of MFIS-type FeFETs. The core part of the scheme is the EKAI model.

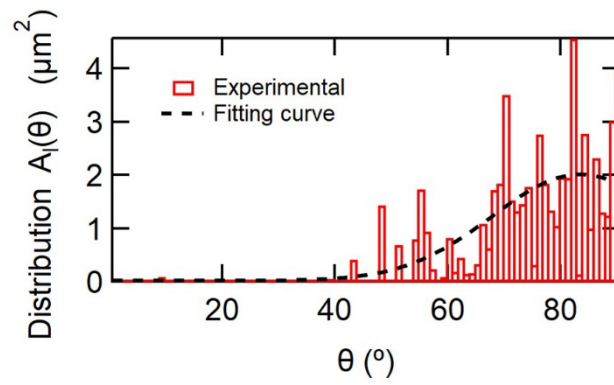
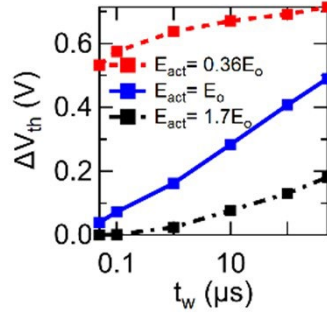
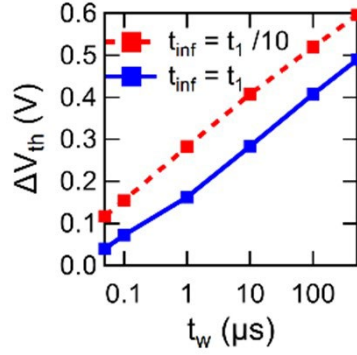


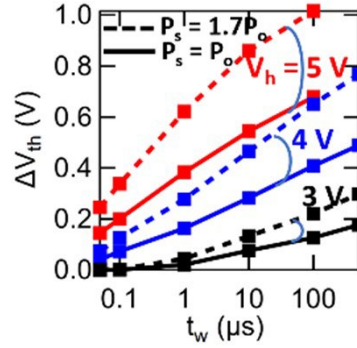
FIG. 7 Area distribution *vs.* θ of CSBT crystal orientations. The EBSD technique derived the distribution in the polycrystalline ferroelectric CSBT layer, constituting the MFIS stack in the Ir/CSBT/I/Si FeFETs. The vertical quantity of the bar graph is the total area of the grains whose angle is in the range from θ to $\theta + \Delta\theta$ ($\Delta\theta$: the bar width). The dashed line is a smoothing curve of the bar graph used in the model calculation.



(a)



(b)



(c)

FIG. 8 Graphs explaining how the parameters, E_{act} , t_{inf} , and P_s , are determined when we compare the model calculations to experimental PWVR data. (a), (b) and (c) show E_{act} , t_{inf} , and P_s dependences of ΔV_{th} vs. t_w curves, respectively. As shown in (a), if E_{act} is not optimized, the log-linear relation of ΔV_{th} vs. t_w cannot be derived across the t_w wide range from 50 ns to 1 ms. (b) indicates that t_{inf} variation brings a parallel shift of ΔV_{th} vs. $\log(t_w)$ curves. (c) indicates that the separation of ΔV_{th} vs. t_w lines at $V_h = -V_l = 3V, 4V$, and $5V$ is very sensitive to P_s . The line separation by the dashed lines is larger than the solid lines, where the former P_s is 1.7 times larger than the latter. E_o in (a), t_1 in (b), and P_o in (c) are example constants for explanation convenience.

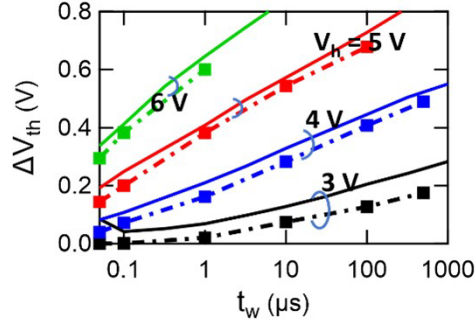


FIG. 9 Model calculation compared to the experimental data regarding PWVR. Dash-and-dot lines are the results of the calculation. Solid lines are the results of the experiment (FIG. A4). The points at the filled square markers on the ΔV_{th} vs. t_w plane are the actual calculation points. Write pulse height conditions are $V_h = -V_l = 3, 4, 5,$ and 6 V. The calculation results agree fairly well with the experimental ones. In particular, the calculation reproduces the log-linear characteristics well. The significant three parameters are $E_{act} = 828$ kV/cm, $t_{inf} = 8.30 \times 10^{-12}$ s, and $P_s = 3.0$ $\mu\text{C}/\text{cm}^2$. Other parameters used for the calculation is summarized as $\sigma = 1, n = 1.3, V_{fb} = -0.8$ V, $d_f = 135$ nm, $\epsilon_{fdi} = 180, d_i = 3.5$ nm, $\epsilon_i = 3.9, D_{it} = 4 \times 10^{12}/\text{Vcm}^2, N_A = 1 \times 10^{16}/\text{cm}^3, \epsilon_s = 11.9, n_i = 1.45 \times 10^{10}$ cm^{-3} , and $T = 300$ K.

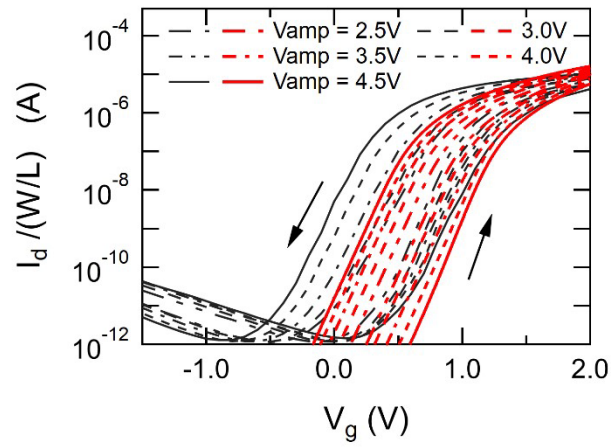


FIG. 10 Model calculation with the experiment (FIG. A1) of quasi-static I_d vs. V_g measurements for various V_g sweep amplitude. Red lines and dark grey lines are the calculation and experiment results, respectively. We used the same parameters as those for PWVR calculation in FIG. 9.

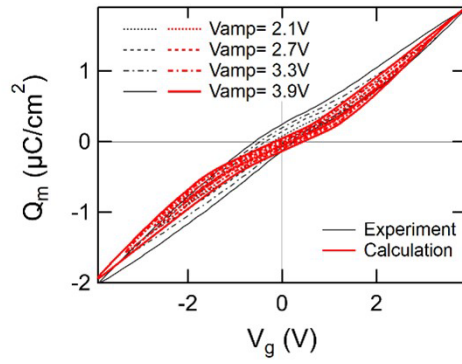
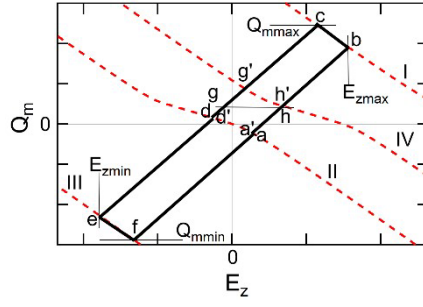
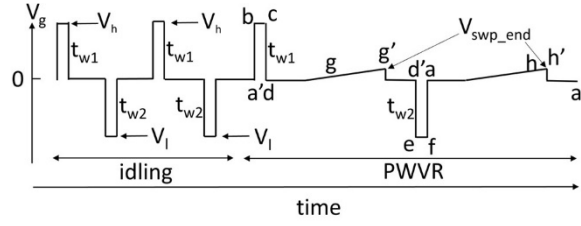


FIG. 11 Model calculation with the experiment (FIG. A2) of quasi-static Q_m vs. V_g measurements for various V_g sweep amplitude. Thicker red lines and dark grey lines are the results of calculation and experiment, respectively. The same parameters as those for PWVR, I_d vs. V_g calculations in FIG. 9 and FIG. 10 were used.



(a)



(b)

FIG. 12 (a) Solid-line loop is the trajectory on Q_m - E_z plane during a PWVR operation, and (b) V_g variation diagram for explanation. Letters from **a** to **h** with **a'**, **d'**, **g'**, and **h'** are checkpoints commonly found in (a) and (b). When a point indexed by a letter represents a state on the V_g vs. time diagram in (b), the ferroelectric state takes the state on the point indexed by the same letter in the solid-line loop in (a). For a step-function-like abrupt change of V_g such as **a'-b**, **c-d**, **d'-e**, or **f-a**, Q_m varies instantaneously on a line whose gradient is $\epsilon_o \epsilon_f d_i$. During a constant V_g application like **b-c** or **e-f**, the Q_m - E_z trajectory follows the load line I or III, $Q_m = -C_i d_f (E_z - (V_g - V_{fb} - \psi_s)/d_f)$. $R_{dn}(l)$ grows on **b-c** according to Eq. (19), and $R_{up}(l)$ grows on **e-f** according to Eq. (22) by the EKAI. The line **d-g-g'-d'** or **a-h-h'-a'** corresponds to data retention (or holding) and V_{th} read stage. At the read end, Q_m rises to **g'** or **h'**. At the retention stage the trajectory also exists on the load line II, $Q_m = -C_i d_f (E_z - (-V_{fb} - \psi_s)/d_f)$. Due to the presence of an electric field, the polarization may be decreased, *i.e.*, **d** (or **a**) may move to an inside point **d'** (or **a'**) on the load line at $V_g = 0$. The decreasing extent depends on E_{act} , E_z , $\cos(\theta_l)$, and the time length between **d** and **d'** (or **a** and **a'**). Q_m rising to **h'** for the read operation may also decrease the polarization.

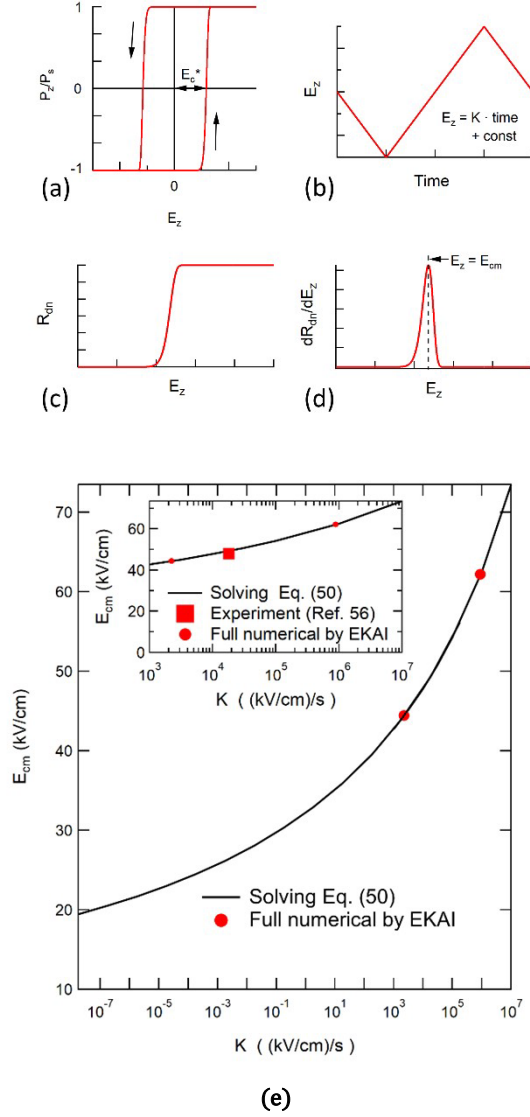
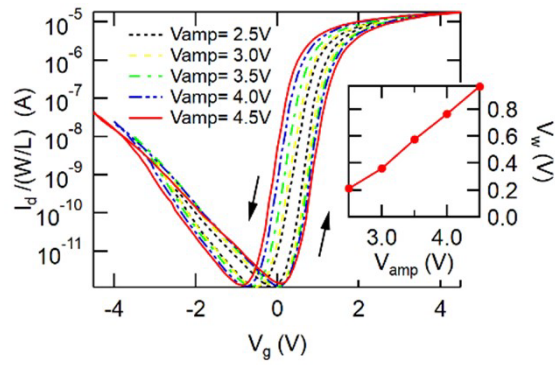
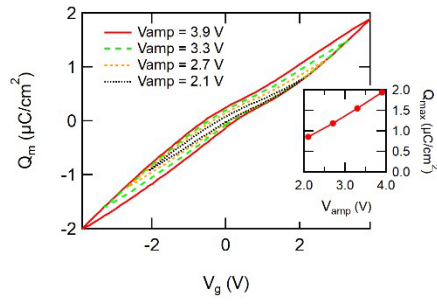


FIG. 13 Semi-analytical discussion of a quantity equivalent to a coercive field in the EKAI model. For an MFM with a single grain ferroelectric, schematic curves of (a) P_z/P_s vs. E_z , (b) triangular waveform $E_z(t)$, (c) R_{dn} vs. E_z , and (d) dR_{dn}/dE_z vs. E_z . The slope, dE_z/dt , is $\pm K$. Since the field (E_{cm}) at which dR_{dn}/dE_z takes a maximum is very close to the coercive field (E_c^*) defined as the field at $Q_m = 0$, E_{cm} can be regarded as a coercive field. An analytical equation, Eq. (50), is derived, the root of which is E_{cm} . The solid lines in (e) and the inset of (e) are the root curve of Eq. (50) as a function of K . The inset in (e) is the graph in the range of $10^3 < K < 10^7$. For usual $Q_m - E_z$ measurement, K is within this range. The filled circles are the E_c^* values obtained by the full numerical calculation of the EKAI and scheme (FIG. 6), and the filled square mark in the inset is the experimental result of SBT [63]. The solid line in (e) indicates that E_{cm} is maintained as about 20 kV/cm under an ultraslow rate $K = 5.5 \times 10^{-8}$ (kV/cm)/s, corresponding that E_z of ± 225 kV/cm sweeping is executed by spending 8×10^9 s.



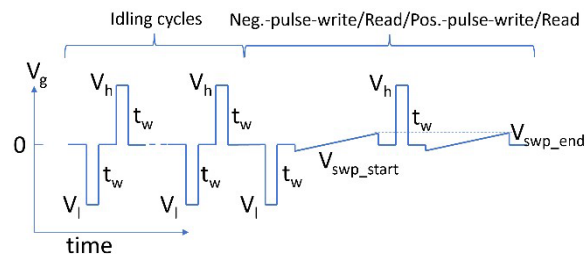
(FIG14)

FIG. A1 Experimental I_d vs. V_g characteristics of an Ir/CSBT/I/Si FeFET at various V_{amp} . V_g was swept between $\pm V_{amp}$ with $V_d = 0.1$ V. Insulator I is the bilayer of HfO_2 layer and SiO_2 -like IL layer. The thickness is 135 nm, 5 nm, and 2.6 nm for CSBT, HfO_2 , and IL, respectively. The I_d that is normalized to W/L is shown in the figure. $L = 10 \mu\text{m}$ and $W = 80 \mu\text{m}$. The small window in the figure shows in the figure V_w vs. V_{amp} , where $V_w = V_{thr} - V_{thl}$, and V_{thr} (V_{thl}) is the V_g value at $I_d/(W/L) = 10^{-8}$ A of the right- (left-) side branch of the hysteresis curves.



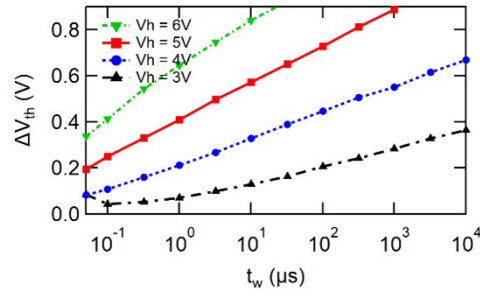
(FIG 15)

FIG. A2 Experimental Q_m vs. V_g characteristics for Ir/CSBT/I/Si FeFET for various V_{amp} . V_g was swept between $\pm V_{amp}$. The stack material and thickness of each layer are the same as those of the FeFET in Fig. A1. $Q_m = Q_{max}$ at $V_g = V_{amp}$, and $Q_m = Q_{min}$ at $V_g = -V_{amp}$. $Q_{max} \cong -Q_{min}$. Q_{max} vs. V_{amp} is shown in the small window on the right side.



(FIG 16)

FIG. A3 Diagram of V_g vs. time used for the experimental PWVR measurement. For a set of V_h , V_l , and t_w , after plural times repeating the idling cycle by the (V_l, t_w) and (V_h, t_w) pulses, the procedure of V_l (<0) pulse write, V_{th} read, V_h pulse write, and V_{th} read was performed.



(FIG 17)

FIG. A4 ΔV_{th} vs. t_w for the experimental Ir/CSBT/I/Si FeFET. The stack material and thickness of each layer are the same as those of the FeFET in Figs. A1 and A2. t_w was changed from 50 ns to 10 ms, with $V_h = -V_l = 3$ V, 4 V, 5 V, 6 V for writing. $V_{swp_start} = 0$ V, $V_{swp_end} = 1.4$ V, and $V_d = 0.1$ V for reading. The markers in the graph are to show measured results. The lines connecting the markers show log-linear relationships of ΔV_{th} and t_w . In particular, the line for $V_h = 4$ V indicates the log-linear line across more than five orders of t_w .